https://doi.org/10.5194/gmd-2021-106
Preprint. Discussion started: 28 May 2021

Geoscientific Model Development Discussions

Variational inverse modelling within the Community Inversion Framework to assimilate $\delta^{13}C(CH_4)$ and CH_4 : a case study with model LMDz-SACS

Joël Thanwerdas[1,*], Marielle Saunois[1], Antoine Berchet[1], Isabelle Pison[1], Bruce H. Vaughn[2], Sylvia Englund Michel[2], and Philippe Bousquet[1]

[1]Laboratoire des Sciences du Climat et de l'Environnement, CEA-CNRS-UVSQ, IPSL, Gif-sur-Yvette, France.
[2]INSTAAR - University of Colorado, Boulder, CO, United States

Correspondence: J. Thanwerdas (joel.thanwerdas@lsce.ipsl.fr)

Abstract.

Atmospheric CH_4 mixing ratios resumed their increase in 2007 after a plateau during the period 1999-2006, suggesting varying sources and sinks as main drivers. Estimating sources by exploiting observations within an inverse modeling framework (top-down approaches) is a powerful approach. It is nevertheless challenging to efficiently differentiate co-located emission categories and sinks by using CH_4 observations alone. As a result, top-down approaches are limited when it comes to fully understanding CH_4 burden changes and attribute these changes to specific source variations. CH_4 source isotopic signatures differ between emission categories (biogenic, thermogenic and pyrogenic), and can therefore be used to address this limitation. Here, a new 3-D variational inverse modeling framework designed to assimilate $\delta^{13}C(CH_4)$ observations together with CH_4 observations is presented. This system is capable of optimizing both emissions and associated source signatures of multiple emission categories at the pixel scale. We present the technical implementation of joint CH_4 and $\delta^{13}C(CH_4)$ constraints in a variational system, and analyze how sensitive the system is to the setup controlling the optimization using the 3-D Chemistry-Transport Model LMDz-SACS. We find that assimilating $\delta^{13}C(CH_4)$ observations and allowing the system to adjust source isotopic signatures provide relatively large differences in global flux estimates for wetlands (5 $\mathrm{Tg\,yr^{-1}}$), microbial (6 $\mathrm{Tg\,yr^{-1}}$), fossil fuels (8 $\mathrm{Tg\,yr^{-1}}$) and biofuels-biomass burning (4 $\mathrm{Tg\,yr^{-1}}$) categories compared to the results inferred without assimilating $\delta^{13}C(CH_4)$ observations. More importantly, when assimilating both CH_4 and $\delta^{13}C(CH_4)$ observations, but assuming source signatures are perfectly known, increase these differences between the system with CH_4 and the enhanced one with $\delta^{13}C(CH_4)$ by a factor 3 or 4, strengthening the importance of having as accurate as possible signatures. Initial conditions, uncertainties on $\delta^{13}C(CH_4)$ observations or the number of optimized categories have a much smaller impact (less than 2 $\mathrm{Tg\,yr^{-1}}$).

1 Introduction

Methane (CH_4) is a powerful greenhouse gas and is responsible for 23 % (Etminan et al., 2016) of the radiative forcing induced by the well-mixed greenhouse gases (CO_2, CH_4, N_2O). Atmospheric CH_4 mixing ratios have increased quasi-continuously since the pre-industrial era and by about 9 ppb/yr from 1984 to 1998 (www.esrl.noaa.gov/gmd/ccgg/trends_ch4/). After a

https://doi.org/10.5194/gmd-2021-106
Preprint. Discussion started: 28 May 2021

Geoscientific Model Development Discussions

plateau between 1999 and 2006 that still generates attention and controversy (e.g., Fujita et al., 2020; Thompson et al., 2018; McNorton et al., 2018; Turner et al., 2017; Schaefer et al., 2016; Schwietzke et al., 2016; Rice et al., 2016), the mixing ratios resumed their increase at a large rate, exceeding 10 ppb/yr in 2014 and 2015. Trends in atmospheric CH_4 are caused by a small imbalance between large sources and sinks. Assessing their spatio-temporal characteristics is particularly challenging considering the variety of methane emissions. Yet, identifying and quantifying the processes contributing to these changes is mandatory to formulate relevant CH_4 mitigation policies that would contribute to meet the target of the 2015 UN Paris Agreement on Climate Change and to limit climate warming to 2 °C.

Thanks to continuous efforts of surface monitoring networks, the spatial coverage and the accuracy of the atmospheric methane measurements provided to the scientific community increased over the last decades. Consequently, top-down estimates using inversion methods emerged and became relevant, along with bottom-up estimates, to explain and quantify the recent sources and sinks variations. The first inverse modeling techniques were designed in the late 1980s and early 1990s for inferring greenhouse gas sources and sinks from atmospheric CO_2 measurements (Enting and Newsam, 1990; Newsam and Enting, 1988). The inverse problem is considered as "ill-posed" (non-uniqueness of the solution, no continuity with the data) and therefore necessitates as many constraints as possible to be regularized. Several methods have been designed over the years, among which analytical (e.g., Bousquet et al., 2006; Gurney et al., 2002), ensemble (e.g., Zupanski et al., 2007; Peters et al., 2005) and variational methods (e.g., Chevallier et al., 2005). The variational formulation uses the adjoint equations of a specific model to compute the gradient of a cost function and then minimize it, for example using a gradient descent method. Computational times and memory costs do not scale with the number of measurements and the number of variables to control, contrary to the analytical and ensemble methods, which can hardly accommodate very large observational datasets and control vectors at the same time. Thus, the variational formulation is preferred to the others when optimizing emissions and sinks at the pixel scale using large volumes of observational data, although its main limitation is the numerical cost to access posterior uncertainties.

Inversion systems generally assimilate measurements from ground-based stations and/or satellites to constrain the global sources and sinks of CH_4, starting from a prior knowledge of these. These systems are very effective to provide total emission estimates (e.g., Saunois et al., 2020; Bergamaschi et al., 2018, 2013; Saunois et al., 2017; Houweling et al., 2017, and references therein). However, differentiating the contributions of multiple co-located CH_4 source categories is challenging as it only relies on different seasonality cycles and on applied spatial distributions and error correlations (e.g., Bergamaschi et al., 2013, 2010). The atmospheric isotopic signal contains additional information on methane emissions that can help to separate emission categories based on their source origin. The atmospheric isotopic signal $\delta^{13}C(CH_4)$ is defined as:

$$\delta^{13}C(CH_4) = \frac{R}{R_{std}} - 1 \quad (1)$$

where R and R_{std} denote the sample and standard $^{13}CH_4$:$^{12}CH_4$ ratios. We use the VPDB scale with R_{std} = 0.00112372 (Craig, 1957) throughout this paper. CH_4 source isotopic signatures $\delta^{13}C(CH_4)_{source}$ notably differ between emission categories ranging from ^{13}C-depleted biogenic sources (approx. -62 ‰) and thermogenic sources (approx. -44 ‰) to ^{13}C-enriched thermogenic sources (approx. -22 ‰) (Sherwood et al., 2017; Schwietzke et al., 2016). Consequently, $\delta^{13}C(CH_4)$ depends on

https://doi.org/10.5194/gmd-2021-106
Preprint. Discussion started: 28 May 2021

Geoscientific Model Development Discussions

both the CH_4 emissions and their isotopic signatures. Saunois et al. (2017) pointed out that many emission scenarios inferred from atmospheric inversions are not consistent with $\delta^{13}C(CH_4)$ observations and that this constrain must be integrated into the inversion systems to avoid such inconsistencies. Since the 1990s, $\delta^{13}C(CH_4)$ have been monitored at multiple sites, although less than for total CH_4, providing opportunities to use this constraint within an inversion framework. In addition, these values have been shifting towards smaller values since 2006 (Nisbet et al., 2019) when CH_4 trends resumed their increase, suggesting that this isotopic data can help to understand the processes that contributed to the regrowth. However, implementing the assimilation of such measurements into an inversion system is not straightforward and introduces additional complexity.

Hereinfafter, the assimilation of $\delta^{13}C(CH_4)$ observations to constrain the estimates of an inversion is referred to as the "isotopic constraint". The implementation of such a constraint in an inversion system have already been attempted in previous studies focusing on CH_4 (e.g., Thompson et al., 2018; McNorton et al., 2018; Rigby et al., 2017; Rice et al., 2016; Schaefer et al., 2016; Schwietzke et al., 2016; Rigby et al., 2012; Neef et al., 2010; Bousquet et al., 2006; Fletcher et al., 2004) but, to our knowledge, never in a variational system. Adding this isotopic constraint to a variational inversion system is challenging as, in contrast to an analytic inversion in which the response functions of the model are precomputed, the isotopic constraints have to be considered both in the forward (simulated isotopic values) and the adjoint (sensitivity of isotopic observations to optimized variables) versions of the model.

The purpose of this study is to present the technical implementation of the isotopic constraint in a variational inversion system and to investigate the sensitivity of this new configuration to different parameters. Our aim is not to estimate trends in sectoral emissions over the last two decades : future studies will address the estimation of CH_4 sources over longer periods of time using this new system. The technical implementation and the various tested configurations are presented in Sect. 2. We analyze the results in Sect.3. Sect. 4 presents our conclusions and recommendations on using such a multi-constraint variational system.

2 Methods

2.1 Theory of variational inversion

The notations introduced here follow the convention defined by Ide et al. (1997). The observation vector is called $\mathbf{y}^o$. It includes here all available observations, namely CH_4 and $\delta^{13}C(CH_4)$ measurements retrieved by surface stations, over the full simulation time-window (see Sect. 2.4.2). The associated errors are assumed to be unbiased and Gaussian and are described within the error covariance matrix $\mathbf{R}$. This matrix accounts for all errors contributing to mismatches between simulated and observed values. $\mathbf{x}$ is the control vector and includes all the variables (here CH_4 surface fluxes, initial CH_4 mixing ratios, source signatures $\delta^{13}C(CH_4)_{source}$ and initial $\delta^{13}C(CH_4)$ values) optimized by the inversion system. Hereinafter, these variables will be referred to as the "control variables". Prior information about the control variables are provided by the vector $\mathbf{x}^b$. Its associated errors are also assumed to be unbiased and Gaussian and are described within the error covariance matrix $\mathbf{B}$. $\mathcal{H}$ is the observation operator that projects the control vector $\mathbf{x}$ into the observation space. This operator mainly consists of the 3-D Chemistry-Transport Model (CTM) (here LMDz-SACS introduced in Sect 2.2). Nevertheless, the CTM is followed by spatial and time operators,

https://doi.org/10.5194/gmd-2021-106
Preprint. Discussion started: 28 May 2021

Geoscientific Model Development Discussions

which interpolate the simulated fields to produce simulated equivalents of the assimilated observations at specific locations and times, making the simulations and observations comparable. An additional 'transformation' operator, implemented in the new system, enables comparison between distinct simulated tracers, e.g. $^{12}CH_4$ and $^{13}CH_4$, and observations, e.g. $\delta^{13}C(CH_4)$ (see Sect 2.3).

In a variational formulation of the inference problem that allows for $\mathcal{H}$ non-linearity, the cost function J is defined as :

$$J(\mathbf{x}) = \frac{1}{2}(\mathbf{x}-\mathbf{x}^{\mathrm{b}})^{\mathrm{T}}\mathbf{B}^{-1}(\mathbf{x}-\mathbf{x}^{\mathrm{b}}) + \frac{1}{2}(\mathcal{H}(\mathbf{x})-\mathbf{y}^{\mathrm{o}})^{T}\mathbf{R}^{-1}(\mathcal{H}(\mathbf{x})-\mathbf{y}^{\mathrm{o}}) \quad (2)$$

$$= J_b(\mathbf{x}) + J_o(\mathbf{x}) \quad (3)$$

The cost function is therefore a sum of two parts :

- The first part is induced by the differences between the posterior and prior variables (J_b).
- The second is induced by the differences between simulations and observations (J_o)

The minimum of J can be reached iteratively with a descent algorithm that requires several computations of the gradient of J with respect to the control vector $\mathbf{x}$:

$$\nabla J_{\mathbf{x}} = \mathbf{B}^{-1}(\mathbf{x}-\mathbf{x}^{\mathrm{b}}) + \mathcal{H}^{*}(\mathbf{R}^{-1}(\mathcal{H}(\mathbf{x})-\mathbf{y}^{\mathrm{o}})) \quad (4)$$

$\mathcal{H}^{*}$ denotes the adjoint operator of $\mathcal{H}$. Although the variational method is a powerful approach for dealing with large numbers of observations and control variables (several hundred thousands), it implies the inversion of both error matrices $\mathbf{R}$ and $\mathbf{B}$. In most applications, R is considered diagonal as point observations are distant in time and space, allowing inversing it easily, although that assumption may change with the increasing availability of satellite sources (Liu et al., 2020). B is rarely diagonal due to spatial and temporal correlations of errors in the fluxes. However, B is often decomposed as combinations of smaller matrices, e.g., using Kronecker products of sub-correlation matrices, which allows to compute its inverse by blocks.

2.2 The Chemistry-Transport Model

The LMDz General Circulation Model (GCM) is the atmospheric component of the Institut Pierre-Simon Laplace Coupled Model (IPSL-CM) developed at the Laboratoire de Météorologie Dynamique (LMD) (Hourdin et al., 2006). The version of LMDz we use is an 'offline' version dedicated to the inversion framework created by Chevallier et al. (2005): precomputed air mass fluxes provided by the online version of LMDz are given as inputs to the transport model, reducing significantly the computational time. The model is set up at a horizontal resolution of 3.8° x 1.9° (96 grid cells in longitude and latitude) with 39 hybrid sigma-pressure levels reaching an altitude up to about 75 km. About 20 levels are dedicated to the stratosphere and the mesosphere. The model time-step is 30 min and the output mixing ratios are 3-hourly snapshots. The horizontal winds are nudged towards ECMWF meteorological analyses (ERA-Interim) in the online version of the model then fed to the offline version. Vertical diffusion is parameterized by a local approach from Louis (1979), and deep convection processes are parameterized by the Tiedtke (1989) scheme.

https://doi.org/10.5194/gmd-2021-106
Preprint. Discussion started: 28 May 2021


Geoscientific Model Development Discussions

The offline model LMDz is coupled with the Simplified Atmospheric Chemistry System (SACS) (Pison et al., 2009). This chemistry system was previously used to simulate the oxidation chain of hydrocarbons, including CH_4, formaldehyde (CH_2O), carbon monoxide (CO) and molecular hydrogen (H_2) together with methyl chloroform (MCF). For the purpose of this study, this system has been converted into a chemistry parsing system. It follows the same principle as the one used by the regional model CHIMERE (Menut et al., 2013) and therefore allows for user-specific chemistry reactions. As a result, it generalizes the previous SACS module to any possible set of reactions. The adjoint code has also been implemented to allow variational inverse modelling. The different species are either prescribed (here OH, O(^{1}D) and Cl) or simulated (here $^{12}CH_4$ and $^{13}CH_4$). The prescribed species are not transported in LMDz, nor are their mixing ratios updated through chemical production or destruction. Such species are only used to calculate reaction rates to update simulated species at each model time step. In this study, the isotopologues $^{12}CH_4$ and $^{13}CH_4$ are simulated as separate tracers and CH_4 is defined as the sum of both isotopologues. Cl + CH_4 oxidation has been implemented to complete the chemical removal of CH_4, which previously only accounted for OH + CH_4 and O(^{1}D) + CH_4 in the SACS scheme. Fractionation values (KIE for Kinetic Isotope Effect) are prescribed to the different sinks. Here, KIE is defined by $\mathrm{KIE} = k_{12}/k_{13}$ where k_{12} is the constant rate of the reaction involving $^{12}CH_4$ and k_{13} is the constant rate of the same reaction involving $^{13}CH_4$. Additional information is provided in the supplement (Text S2). The chemistry-transport LMDz-SACS is used to test the new variational inverse modelling system that is described in the next section.

2.3 Technical implementation of the isotopic constraint

The isotopic multi-constrain system was implemented in the Community Inversion Framework (CIF), supported by the European Union H2020 project VERIFY (http://www.community-inversion.eu). The CIF has been designed to allow comparison of different approaches, models and inversion systems used in the inversion community (Berchet et al., 2020). Different atmospheric transport models, regional and global, Eulerian and Lagrangian are implemented within the CIF. The system presented in this paper has been originally designed to run and be tested with LMDz-SACS but can theoretically be coupled with all models implemented in the CIF framework. The system is able to :

- Assimilate $\delta^{13}C(CH_4)$ and CH_4 observations together.
- Independently optimize fluxes and isotopic signatures for multiple emission categories.
- Optimize $\delta^{13}C(CH_4)$ and CH_4 initial conditions.

Figure 1 shows the different steps of a minimization iteration of the cost function. Each iteration performed with the descent algorithm can be decomposed into four main steps presented below. For clarity, we only present here the optimization of CH_4 fluxes and associated source signatures but CH_4 and $\delta^{13}C(CH_4)$ initial conditions can also be optimized by the system following the same process.

https://doi.org/10.5194/gmd-2021-106
Preprint. Discussion started: 28 May 2021

Geoscientific Model Development Discussions

1. The process starts with a forward run. The different flux variables are extracted and converted into $^{12}CH_4$ and $^{13}CH_4$ mass fluxes for each category following the Eq. (5)-(7) below.

$$A^i = (1 + \delta^{13}C(CH_4)^i_{\text{source}}) \cdot R_{std} \tag{5}$$

$$F^i_{12} = \frac{M_{12}}{M_{TOT}} \cdot \frac{1}{1 + A^i} \cdot F^i_{TOT} \tag{6}$$

$$F^i_{13} = \frac{M_{13}}{M_{TOT}} \cdot \frac{A^i}{1 + A^i} \cdot F^i_{TOT} \tag{7}$$

F^i_{TOT}, F^i_{12} and F^i_{13} are the CH_4, $^{12}CH_4$ and $^{13}CH_4$ fluxes in $\text{kg}\,\text{m}^{-2}\,\text{s}^{-1}$ of a specific category i, respectively. M_{TOT}, M_{12} and M_{13} are the CH_4, $^{12}CH_4$ and $^{13}CH_4$ molar masses, respectively. $\delta^{13}C(CH_4)^i_{\text{source}}$ is the source isotopic signature of the category i.

The $^{12}CH_4$ and $^{13}CH_4$ fluxes are then provided by summing all categories and used by the model LMDz-SACS to simulate the $^{12}CH_4$ and $^{13}CH_4$ atmospheric mixing ratios over the time-window considered. Finally, the simulated values are converted back to CH_4 and $\delta^{13}C(CH_4)$ simulated equivalent of the assimilated observations using Eq. (8) and (9) below :

$$[CH_4] = [^{12}CH_4] + [^{13}CH_4] \tag{8}$$

$$\delta^{13}C(CH_4) = \frac{[^{13}CH_4]}{[^{12}CH_4]} \cdot \frac{1}{R_{std}} - 1 \tag{9}$$

$[CH_4]$, $[^{12}CH_4]$ and $[^{13}CH_4]$ are CH_4, $^{12}CH_4$ and $^{13}CH_4$ atmospheric mixing ratios simulated by the model in $\text{mol}\,\text{mol}^{-1}$, respectively.

2. These simulated values are then compared to the available observations in order to compute $\mathcal{H}(\mathbf{x}) - \mathbf{y}^{\text{o}}$ which is further used to infer the cost function and generate CH_4 and $\delta^{13}C(CH_4)$ adjoint forcings (indicated by the "*" star superscript symbol) that compose the vector $\delta\mathbf{y}^*$:

$$\delta\mathbf{y}^* = \mathbf{R}^{-1}(\mathcal{H}(\mathbf{x}) - \mathbf{y}^{\text{o}}) \tag{10}$$

This vector is normally used directly as input to the adjoint model (see Eq. 4) but in the new system, the adjoint forcings CH_4 and $^{13}C(CH_4)$ must first be converted into the adjoint forcings $^{12}CH_4$ and $^{13}CH_4$.

3. The newly designed adjoint code that converts CH_4 and $\delta^{13}C(CH_4)$ adjoint forcings into $^{12}CH_4$ and $^{13}CH_4$ adjoint forcings is based on the Eq. (11)-(13) depending on the type of the initial observation.

$$[^{12}CH_4]^*_{CH_4} = [^{13}CH_4]^*_{CH_4} = [CH_4]^* \tag{11}$$

$$[^{12}CH_4]^*_{\delta^{13}C} = -\frac{[^{13}CH_4]}{[^{12}CH_4]^2} \cdot \frac{1}{R_{std}} \cdot \delta^{13}C(CH_4)^* \tag{12}$$

$$[^{13}CH_4]^*_{\delta^{13}C} = \frac{1}{[^{12}CH_4]} \cdot \frac{1}{R_{std}} \cdot \delta^{13}C(CH_4)^* \tag{13}$$

https://doi.org/10.5194/gmd-2021-106
Preprint. Discussion started: 28 May 2021

Geoscientific Model Development Discussions

$[^{12}CH_4]^*_{CH_4}$ and $[^{13}CH_4]^*_{CH_4}$ are adjoint forcings associated with CH_4 observations. $[^{12}CH_4]^*_{\delta^{13}C}$ and $[^{13}CH_4]^*_{\delta^{13}C}$ are adjoint forcings associated with $\delta^{13}C(CH_4)$ observations. The adjoint code of the CTM is then run with these adjoint forcings as inputs.

Outputs of the adjoint run provide the sensitivities of the adjoint forcings to the $^{12}CH_4$ and $^{13}CH_4$ fluxes of a specific category i denoted $F^{*,i}_{12}$ and $F^{*,i}_{13}$. Equations (14) and (15) convert them back to sensitivities to the initial control variables, denoted $F^{*,i}_{TOT}$ and $\delta^{13}C(CH_4)^{*,i}_{\text{source}}$.

$$F^{*,i}_{TOT} = \frac{1}{1+A} \cdot [\frac{M_{12}}{M_{TOT}} \cdot F^{*,i}_{12} + \frac{M_{13}}{M_{TOT}} \cdot A \cdot F^{*,i}_{13}] \tag{14}$$

$$\delta^{13}C(CH_4)^{*,i}_{\text{source}} = R_{std} \cdot \frac{F_{TOT}}{(1+A)^2} \cdot [\frac{M_{13}}{M_{TOT}} \cdot F^{*,i}_{13} - \frac{M_{12}}{M_{TOT}} \cdot F^{*,i}_{12}] \tag{15}$$

4. The minimization algorithm uses these sensitivities to compute the gradient of the cost function. It then finds an optimized control vector that reduces the cost function and that is used for the next iteration.

2.4 Setup of the reference simulation

The reference configuration (REF) is a variational inversion that optimizes the CH_4 emission fluxes and $\delta^{13}C(CH_4)$ source isotopic signatures of five different categories (biofuels-biomass burning, microbial, fossil fuels, natural and wetlands) and the CH_4/$\delta^{13}C(CH_4)$ initial conditions. The assimilation time-window is the period 2012-2017. The five categories originate from an aggregation of ten sub-categories (Table 1) and chosen to be as isotopically consistent as possible. Sinks are not optimized here.

2.4.1 Control vector $\mathbf{x}$ and $\mathbf{B}$ matrix

We adopt the CH_4 emissions compiled for inversions performed as part of the Global Methane Budget (Saunois et al., 2020). Anthropogenic (including biofuels) and fire emissions are based on the EDGARv432 database (http://edgar.jrc.ec.europa.eu/overview.php?v=432&SECURE=123) (Janssens-Maenhout et al., 2017) and the GFED4s databases (van der Werf et al., 2017), respectively. Statistics from British Petroleum (BP) and the Food and Agriculture Organization of the United Nations (FAO) have been used to extend the EDGARv432 database, ending 2012, until 2017. The natural sources emissions are based on averaged literature values : Poulter et al. (2017) for wetlands, Kirschke et al. (2013) for termites, Lambert and Schmidt (1993) for ocean and Etiope (2015) for geological sources. Globally averaged emissions over the period 2012-2017 are listed in Table 1.

Source isotopic signatures are provided either at the pixel scale (for wetlands), at the regional scale based on TransCom regions (Patra et al., 2011) or at the global scale. The wetlands signature map is taken from Ganesan et al. (2018). Livestock source isotopic signatures are taken from Chang et al. (2019) and aggregated into the 11-regions map by selecting region-specific values. These estimates end in 2013, therefore the years 2014 to 2017 are set equal to the year 2013. Coal and Oil, Gas, Industry (OGI) isotopic signature values are inferred from Sherwood et al. (2017) and Zazzeri et al. (2016) and aggregated into

https://doi.org/10.5194/gmd-2021-106
Preprint. Discussion started: 28 May 2021

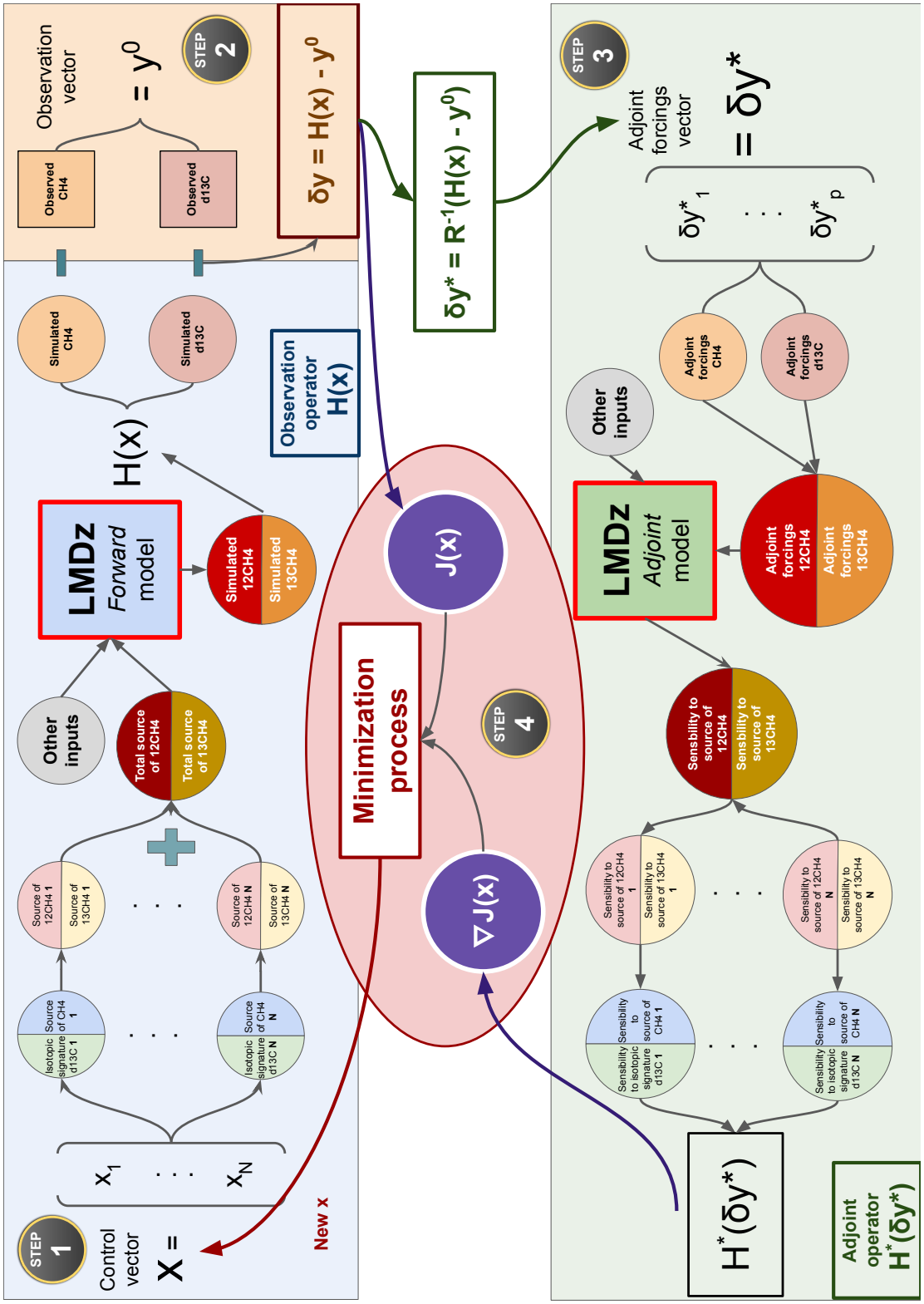

Figure 1. The minimization iteration process in the newly designed system. The "step" black circles with gold border indicates the reading direction to follow. Step 1 (blue rectangle) refers to a forward run. Step 2 (orange rectangle) refers to the forward and adjoint operations required to compare observations and simulated values. Step 3 (green rectangle) refers to an adjoint run. This step must be read from the right to the left. Step 4 (red ellipse) refers to the minimization of the cost function operated by the dedicated minimization algorithm. Note that results of Step 2 are used both in the minimization process (red ellipse) and as inputs for Step 3. The minimization iteration process followed by the previous system is also illustrated in the supplement (Fig. S1)

https://doi.org/10.5194/gmd-2021-106
Preprint. Discussion started: 28 May 2021

Geoscientific Model Development Discussions

Table 1. Emissions and flux-weighted isotopic signatures of the CH_4 sources averaged over 2012-2017 for different categories and their sub-categories. * Unc. : Prior uncertainty in the isotopic signature prescribed to the category or the sub-category. Prior uncertainty in fluxes are set to 100 % for all categories and sub-categories.

Categories	**Emissions** ($Tg\,yr^{-1}$)	**Signature** (‰)	**Unc.*** (%)	**Sub-categories**	**Emissions** ($Tg\,yr^{-1}$)	**Signature** (‰)	**Unc.*** (%)
Wetlands (WT)	180.3	-60.8	20	Wetlands	180.3	-60.8	20
Microbial (MC)	226.4	-59.1	20	Rice cultivation	38.0	-63	20
				Livestock	117.8	-63.6	20
				Waste	70.6	-49.5	20
Fossil Fuels (FF)	116.3	-43.4	25	Coal	38.4	-40.4	25
				Oil, Gas, Industry	77.9	-44.9	25
Biofuels-biomass burning (BB)	28.4	-22.5	40	Biofuels-biomass burning	28.4	-22.5	40
Natural (NAT)	38.1	-49.9	15	Oceans	14.4	-42.0	20
				Termites	8.7	-63.0	20
				Geological (onshore)	15.0	-50.0	20
Total	589.5	-54.1		Total	589.5	-54.1	

the same 11-regions map. As for the biofuels-biomass burning category, we use region-specific signatures over 11 regions. A global signature value is prescribed for each of the other categories. Except for the livestock category, all prior signatures are set constant over time. Additional information regarding the chosen isotopic signatures and their references is provided in the supplement (Text S1).

Three values per month (10 days, 10 days and the rest) for the fluxes and their associated isotopic signatures are included in the control variables. Although the time variations of isotopic signatures are poorly constrained in the literature, we choose to include the same number of variables for fluxes and isotopic signatures in order to illustrate the full capabilities of the system and have it ready when more isotopic constraints will appear.

The portion of the diagonal of $\mathbf{B}$ associated to prior CH_4 emission fluxes is filled in with the variances set to 100 % of the square of the maximum of emissions over the cell and its eight neighbours during each month. Off diagonal terms of $\mathbf{B}$ (covariances) are based on correlation e-folding lengths (500 km over land and 1000 km over sea). The same method is applied for source isotopic signatures, although a specific percentage of uncertainties deduced from Sherwood et al. (2017) is used to infer each category diagonal term (see Table 1). No temporal correlations are considered here. Finally, prior uncertainties on initial conditions are set to 10 % for CH_4 ($\sim$ 180 ppb) and 3 % for $\delta^{13}C(CH_4)$ ($\sim$ 1.4 ‰).

2.4.2 Observation vector y and R matrix

CH_4 observations are taken from the data archived at the World Data Centre for Greenhouse Gases (WDCGG) of the WMO Global Atmospheric Watch (WMO-GAW) program. We selected 66 stations from 13 surface monitoring networks providing

https://doi.org/10.5194/gmd-2021-106
Preprint. Discussion started: 28 May 2021

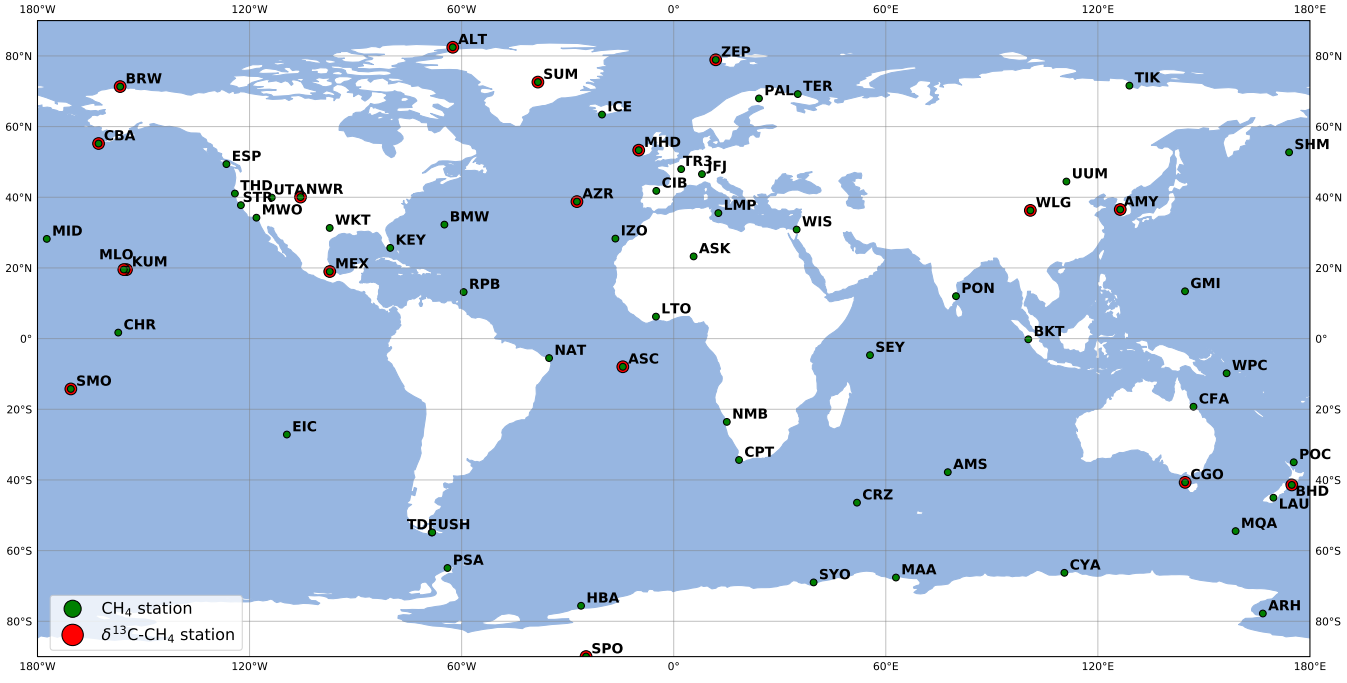

Figure 2. Locations of CH_4 and $\delta^{13}C(CH_4)$ surface stations. Affiliated networks are not displayed. More information can be found in the supplement (Table S3 and S4).

in-situ measurements of CH_4 mixing ratios. The stations are displayed in Fig. 2. Table S3 in the supplement provides a list of these 66 stations and specific information.

$\delta^{13}C(CH_4)$ observations are taken from 18 surface stations from the Global Greenhouse Gas Reference Network (GGGRN), part of NOAA-ESRL Global Monitoring Division (NOAA-ESRL GMD). Air samples have been collected on an approximately weekly basis during the 2012-2017 period and analyzed by the Institute of Arctic and Alpine Research (INSTAAR) to provide $\delta^{13}C(CH_4)$ isotope ratio measurements. The analytical uncertainty of the isotopic measurements is 0.06 ‰. Table S4 in the supplement provides a list of these 18 stations and specific information. The observed high-frequency temporal variability cannot be adequately reproduced by the LMDz-SACS model. Therefore, instead of assimilating the real observations, we used a smooth curve fitting the real observations. The fitting curve is a function including 3 polynomial parameters (quadratic) and 8 harmonic parameters. One sensitivity inversion aims at estimating the error introduced by this simplification (simulation S2 in Table 2).

The $\mathbf{R}$ matrix introduced in Sect. 2.1 is defined as diagonal, assuming that observation errors are not correlated, neither in space nor in time. This diagonal matrix can be decomposed into two parts : measurement and model error variance. Measurement errors account for instrumental errors while model errors encompass transport and representativity errors induced by the

https://doi.org/10.5194/gmd-2021-106
Preprint. Discussion started: 28 May 2021

Geoscientific Model Development Discussions

model :

$$\mathbf{R} = \mathbf{R_{measurement}} + \mathbf{R_{model}} \tag{16}$$

Here, we use the provided observation errors to fill the $\mathbf{R_{measurement}}$ diagonal matrix. Globalview-CH_4 (Globalview-CH_4, 2009) values are used to represent model errors and prescribe variances at each station for CH_4 mixing ratio measurements in order to fill the $\mathbf{R_{model}}$ diagonal matrix. This simple approach has been used previously in atmospheric inversions (Locatelli et al., 2015, 2013; Yver et al., 2011; Bousquet et al., 2006; Rodenbeck et al., 2003). Errors in Globalview-CH_4 are computed at each site as the Root-Mean-Square-Error (RMSE) of the measurements on a smooth curve fitting them. As Globalview-CH_4 does not provide errors for $\delta^{13}C(CH_4)$ measurements, the same method has been applied here. RMSE of the measurements on a smooth curve fitting them over the period 2012-2017 is prescribed as the standard deviation for each site providing $\delta^{13}C(CH_4)$ measurements.

2.4.3 Spin-up

The model has been spun-up during 30 years using constant emissions and recycling meteorology from the year 2012 in order to consider the long timescales for isotopic changes (Tans, 1997). At the end of the spin-up, $\delta^{13}C(CH_4)$ values have been offset to fit the $\delta^{13}C(CH_4)$ global-mean in January 2012 and CH_4 mixing ratios have been scaled to fit the CH_4 global-mean mixing ratios in January 2012. Due to the non-linearity of transport and mixing, offsetting $\delta^{13}C(CH_4)$ initial values in a forward run can generate errors. This impact is discussed later using a configuration where $\delta^{13}C(CH_4)$ initial conditions have not been offset (S1).

2.5 Sensitivity tests

Table 2. Nomenclature and characteristics of the configurations. Details are provided in Sect. 2.5. ** Prior uncertainties on initial $\delta^{13}C(CH_4)$ conditions have been set to 10 %.

Configuration name	$\delta^{13}C(CH_4)$ initial cond.	$\delta^{13}C(CH_4)$ observations	$\delta^{13}C(CH_4)$ model uncertainties	$\delta^{13}C(CH_4)_{source}$ regional variability	$\delta^{13}C(CH_4)_{source}$ uncertainties	Number of categories
NOISO	Without isotopic constraint					5
REF	Offset	Curve fitting	RMSE obs-fit	Regional variability	REF uncertainties	5
S1	No offset**	Curve fitting	RMSE obs-fit	Regional variability	REF uncertainties	5
S2	Offset	Real observations	RMSE obs-fit	Regional variability	REF uncertainties	5
S3	Offset	Curve fitting	RMSE obs-fit / 2	Regional variability	REF uncertainties	5
T1	Offset	Curve fitting	RMSE obs-fit	Regional variability	REF uncertainties	10
T2	Offset	Curve fitting	RMSE obs-fit	Global mean	REF uncertainties	5
T3	Offset	Curve fitting	RMSE obs-fit	Regional variability	1 % for each category	5
T4	Offset	Curve fitting	RMSE obs-fit	Global mean	1 % for each category	5

https://doi.org/10.5194/gmd-2021-106
Preprint. Discussion started: 28 May 2021


Geoscientific Model Development Discussions

Including REF, a set of 9 different configurations has been designed to assess the impact of assimilating $\delta^{13}C(CH_4)$ observations in addition to CH_4 observations and also to evaluate the sensitivity of the inversion results to the system's setup.

Multiple parameters have been tested throughout the various configurations : NOISO has no isotopic constraint. Therefore, this configuration only simulates CH_4 and assimilates CH_4 observations. $\delta^{13}C(CH_4)$ initial conditions in S1 are not offset and are directly taken from the spin-up. S2 assimilates the real $\delta^{13}C(CH_4)$ observations instead of the fitting curve data. In S3, the $\delta^{13}C(CH_4)$ model uncertainties are divided by a factor 2. T1 uses 10 sub-categories instead of 5 aggregated categories, increasing the degrees of freedom. In theory, the system is capable of optimally adjusting two source signatures if the assimilated information is sufficient. For instance, the system can choose to shift one signature downward and another upward in a given pixel, in order to improve the fitting in this specific pixel. The configuration T2 has been specifically designed to investigate whether the system would be able to retrieve a realistic distribution (similar to REF) starting from globally averaged signatures for each category. In T3, the $\delta^{13}C(CH_4)$ source signatures uncertainties are set to a very low value (1 %) in order to prevent the system from optimizing them. In other words, all changes are put on CH_4 emissions. Finally, T4 applies both changes from T2 and T3. Table 2 summarizes the different configurations and the associated changes. The configurations have been grouped into two sets to facilitate the analysis of the results : on the one hand, S-group configurations (REF + S1-S4) have setup variations that are not expected to largely influence the results. On the other hand, T-group configurations (T1-T4) alter parameters that are very likely to impact the results.

3 Results

3.1 Minimization of the cost function

The minimization process is performed using the M1QN3 algorithm (Gilbert and Lemaréchal, 1989). One full simulation (forward + adjoint) necessitates about 170 CPU hours to run 6 years, i.e. 2.4 CPU hours per month simulated. The computational burden is increased by a factor 2 in comparison to an inversion without the isotopic constraint due to the doubling of simulated tracers ($^{12}CH_4$ and $^{13}CH_4$). One full simulation is generally enough to complete one iteration of the minimization process but two or three simulations are sometimes required by M1QN3. Therefore, the number of simulations is slightly larger than the number of iterations. Figure 3 displays the minimization process of the cost function for all configurations.

Except for S1 and T1, the inversions were stopped when the gradient norm reduction exceeded 96% for the third consecutive iteration. Number of iterations are compared to investigate the sensibility of the computational cost to the setup. 32 iterations (37 simulations) for NOISO, 43 iterations (47 simulations) for REF and about 50 iterations for the others were necessary. Consequently, although assimilating $\delta^{13}C(CH_4)$ observations requires at least 11 additional iterations, the setup has little influence on the number of iterations if the same convergence criteria is used.

S1 and T1 inversions were extended until their cost function reached the same reduction as REF in order to estimate the additional computational burden required to reach similar results when initial conditions are not offset (S1) and the number of categories is increased (T1). 10 and 21 additional iterations were necessary for T1 and S1, respectively. For T1, it shows

https://doi.org/10.5194/gmd-2021-106
Preprint. Discussion started: 28 May 2021

Geoscientific Model Development Discussions

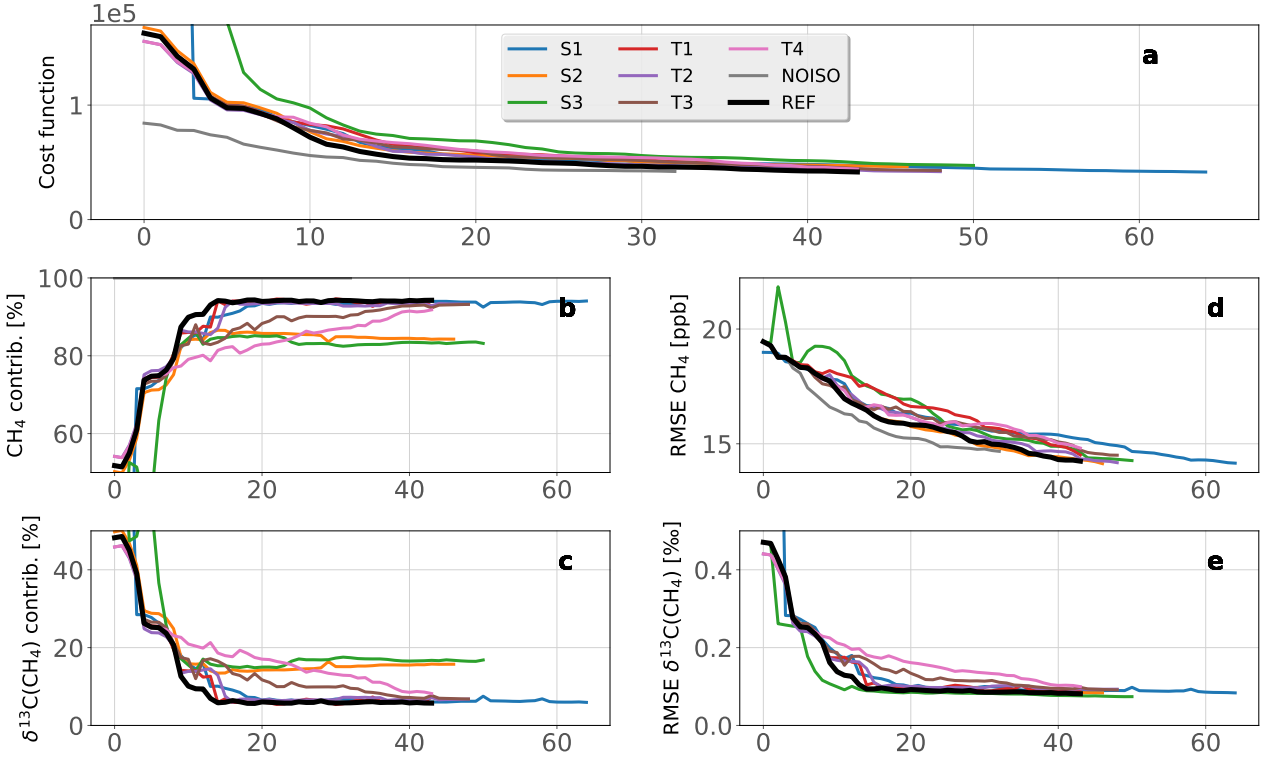

Figure 3. Minimization of the cost function for all configurations. a) Cost function with respect to the number of iterations. b) CH_4 contribution to J_o. c) $\delta^{13}C(CH_4)$ contribution to J_o. d) RMSE associated to observed-simulated CH_4. e) RMSE associated to observed-simulated $\delta^{13}C(CH_4)$. For clarity reasons, S1 and S3 initial values are not displayed because they are too large compared to REF.

that increasing the degrees of freedom also increases the computational burden. For S1, it highlights the benefits of offsetting $\delta^{13}C(CH_4)$ initial conditions.

As we assume no correlation of errors in R, J_o (see Eq. 3) can be divided into CH_4 and $\delta^{13}C(CH_4)$ contributions. Figure 3 shows that all configurations lead to a fast reduction of the $\delta^{13}C(CH_4)$ contribution. During the first ten iterations, it decreased from 50-90% (depending on the configuration) to 10-20 %. Conversely, the CH_4 contribution increased from 10-50 % to 80-90%. By adjusting the source isotopic signatures (all configurations besides T3-T4), the system was able to efficiently and rapidly reduce the discrepancies between simulated and observed $\delta^{13}C(CH_4)$. As a result, the $\delta^{13}C(CH_4)$ RMSE decreased very rapidly during the first ten iterations while the CH_4 RMSE due to CH_4 discrepancies decreased at a roughly constant rate. Consequently, the system is preferentially adjusting $\delta^{13}C(CH_4)$ over CH_4 values to reduce the cost function.

https://doi.org/10.5194/gmd-2021-106
Preprint. Discussion started: 28 May 2021


Geoscientific Model Development Discussions

The decrease rate associated with $\delta^{13}C(CH_4)$ RMSE can be increased by reducing the model uncertainties prescribed to the $\delta^{13}C(CH_4)$ observations. S3 is an example of such an adjustment, as the model uncertainties have been divided by two. With this configuration, the system requires five less iterations than REF to reach similar $\delta^{13}C(CH_4)$ RMSE reduction but 7 additional iterations to reach similar CH_4 RMSE reduction. T3 and T4 configurations constrains the isotopic signatures, thus the reduction of the $\delta^{13}C(CH_4)$ contribution necessitates 25 more iterations than REF to reach similar RMSE reduction. To summarize, the decrease rate associated with $\delta^{13}C(CH_4)$ RMSE is highly dependent on the prescribed uncertainties in $\delta^{13}C(CH_4)$ observations and the ability of the system to adjust source signatures.

3.2 CH_4 and $\delta^{13}C(CH_4)$ fitting

As expected, the assimilation process greatly improves the agreement between simulated and observed values for both CH_4 and $\delta^{13}C(CH_4)$. Figure 4 shows the globally-averaged time-series of CH_4 and $\delta^{13}C(CH_4)$.

CH_4 RMSE using prior estimates is 19.4 ppb and drops to 14.3 $\pm$ 0.2 ppb (1σ) on average over all the configurations using posterior estimates. Prior estimates lead to simulated CH_4 mixing ratios in good agreement with observations and the improvement is therefore relatively small. In addition, all configuration results regarding CH_4 are very similar. In particular, NOISO is not performing much differently than the other configurations, indicating that the additional isotopic constraint does not affect the fitting to CH_4 observations.

Prior $\delta^{13}C(CH_4)$ prescribed in REF are continuously decreasing from -47.2 to -48.2 ‰ and thus agrees very poorly (RMSE is 0.47 ‰) with observed values. This is likely due to an underestimation (too negative values) of some source isotopic signatures or a poor prior estimation of the source partitioning, i.e. an underestimation of ^{13}C-enriched sources (fossil fuels or biomass burning) or an overestimation of ^{13}C-depleted sources (biogenic). The data assimilation process reconciles simulated and observed $\delta^{13}C(CH_4)$ (RMSE is 0.086 $\pm$ 0.008 ‰) for all configurations, albeit small differences depending on the setup emerge.

The S-group provides a better match than the T-group (0.081 $\pm$ 0.003 ‰ versus 0.091 $\pm$ 0.007 ‰). Furthermore, the fit is very similar within the S-group. In contrast, the spread in the T-group is larger with $\delta^{13}C(CH_4)$ RMSE being equal to 0.093 ‰, 0.091 ‰ and 0.099 ‰ respectively for T2, T3 and T4. These results suggest that giving more freedom to the system to adjust the isotopic signatures and providing regional-specific estimates of prior source signatures instead of global values may be key elements for reaching better agreement. Best results (i.e. smallest RMSE) are obtained with T1 (0.079 ‰). However, this configuration necessitates 10 additional iterations to reach better results than REF. Without these additional iterations, REF would be the best configuration (0.081 ‰).

Figure 5 shows the RMSE distribution at all measurement sites for each configuration. All sites exhibit a RMSE reduction (from prior to posterior) for both CH_4 and $\delta^{13}C(CH_4)$, except for BKT with T3 and T4 configurations. Furthermore, BKT, WKT, UUM, AMY and PON exhibit a posterior CH_4 RMSE above 25 ppb, showing that CH_4 measurements retrieved at these stations are not properly reproduced by the model, despite the optimization. It can be due to transport error or misrepresentation of sources close to the sites. Addressing this misfit is beyond the scope of this study, although the configuration influences the results : BKT and UUM fitting are notably deteriorated with T3 and T4 configurations. For example, BKT appears to be

https://doi.org/10.5194/gmd-2021-106
Preprint. Discussion started: 28 May 2021

Geoscientific Model Development Discussions
Open Access
EGU

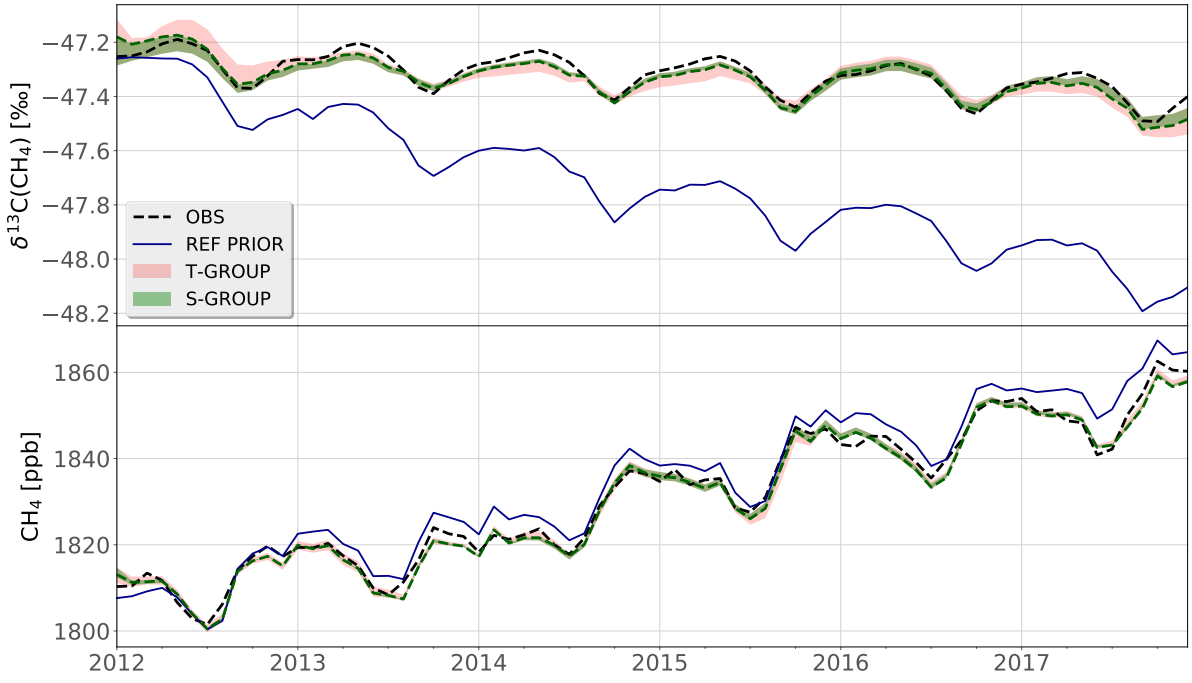

Figure 4. Global-mean CH_4 mixing ratios and $\delta^{13}C(CH_4)$ values between 2012 and 2017. The dashed black and solid blue lines in each panel denote the observed and REF prior estimates, respectively. The red and green ranges show the maximum and minimum values of the T-group and S-group, respectively. The thick and dashed green line denotes the REF configuration. Globally-averaged values are computed using a method similar to Masarie and Tans (1995): a function including 3 polynomial parameters (quadratic) and 8 harmonic parameters is fitted to each time-series at available sites; the final value is obtained by performing a latitude-band weighted average over the Marine Boundary Layer (MBL) sites. The latitude band width was set at 30°.

influenced by biomass burning sources in South-East Asia, which are strongly dependent on the configuration (see Sect. 3.3). Moreover, T3 provides the poorest $\delta^{13}C(CH_4)$ fitting at AMY (0.24 ‰). Therefore, setting global values for source signatures and preventing the system from optimizing them lead to poorer fitting. On the contrary, T1 improves the results, indicating that additional degrees of freedom can help to reconcile simulations with observations, especially in South-East Asia where these stations are located.

3.3 Global and regional emission increments

We are primarily interested in the additional information provided by the assimilation of $\delta^{13}C(CH_4)$ data. Rather than discussing the regional and global CH_4 emissions and comparing these results to previous estimates, we investigate the differences

https://doi.org/10.5194/gmd-2021-106
Preprint. Discussion started: 28 May 2021

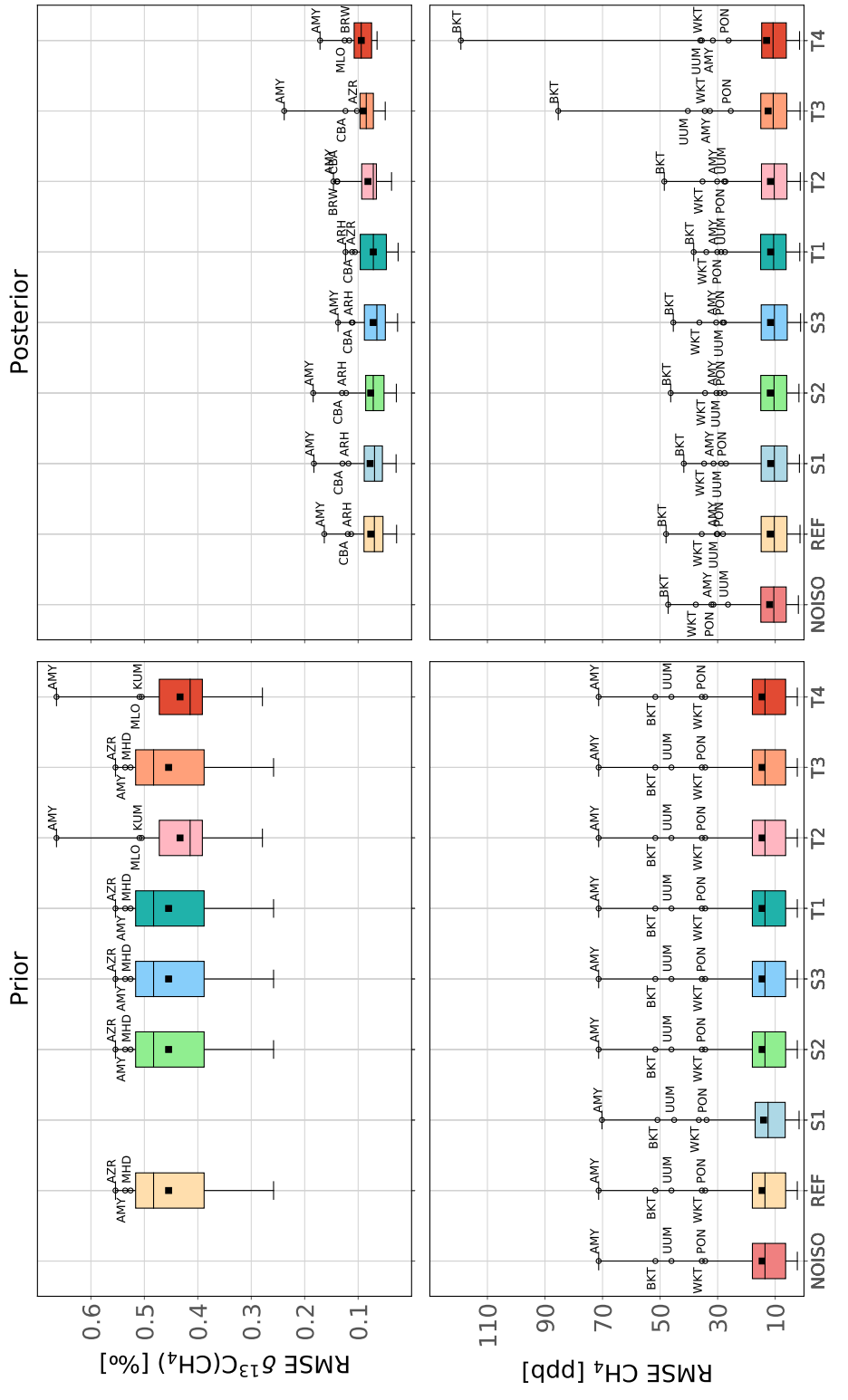

Figure 5. RMSE distribution at the surface stations. Left panels show the prior CH_4 and $\delta^{13}C(CH_4)$ RMSE and right panels show the posterior RMSE. Upper panels show $\delta^{13}C(CH_4)$ RMSE and lower panels show CH_4 RMSE. For clarity reasons, S1 prior is not shown for $\delta^{13}C(CH_4)$ because the prior misfit is much larger than that of the other configurations. The box plot whiskers are covering the whole range of the data.

https://doi.org/10.5194/gmd-2021-106
Preprint. Discussion started: 28 May 2021

Geoscientific Model Development Discussions
Open Access
EGU

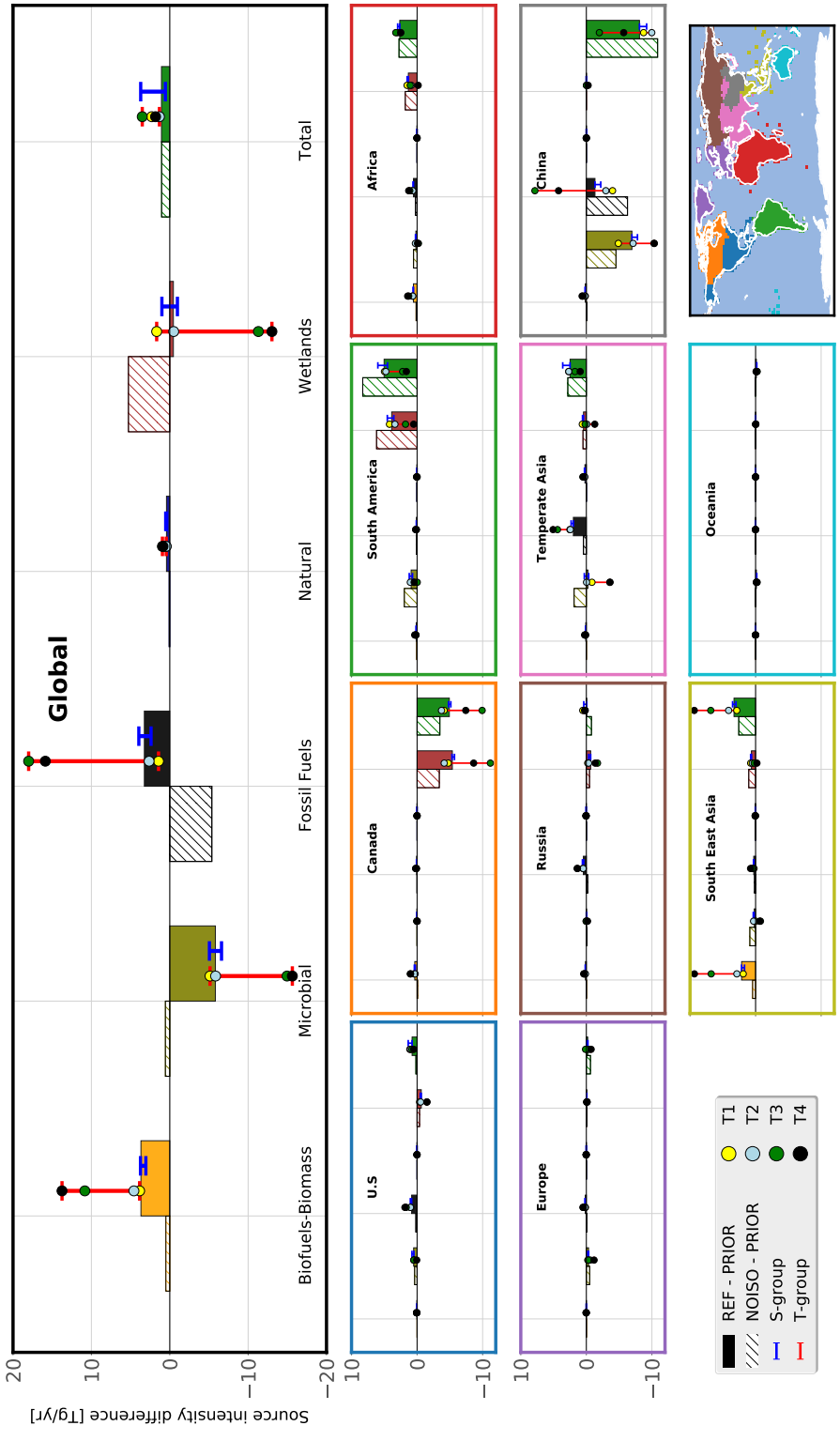

Figure 6. REF and NOISO emission increments for the period 2014-2015. Prior estimates (PRIOR) are identical for both configurations. The color-filled bars show the differences between REF posterior and prior estimates (REF increment). The hatched bars show the differences between NOISO posterior and prior estimates (NOISO increment). The upper panel refers to the global emissions. The lower panels refer to multiple regions of the globe. The regions are shown on the lower right panel. Red and blue error bars represent the minimum and maximum of the T-group and S-group, respectively. Circles on the red error bar show the results from the T-group.

https://doi.org/10.5194/gmd-2021-106
Preprint. Discussion started: 28 May 2021


Geoscientific Model Development Discussions
Open Access
EGU

between emissions inferred from configurations with and without the additional isotopic constraint. Long-term inversions will be run in the future with this system to provide more robust estimates of CH_4 emissions and compare them to the existing literature.

The inversion time-window is the period 2012-2017. However, flux and source signature estimations of the 2012-2013 and 2016-2017 periods are not interpreted as the system appears to require a 2-year spin-up (2012-2013) and a 2-year spin-down (2016-2017), over which the inversion problem is not sufficiently constrained and isotopic signatures vary widely over time. Therefore, only the 2014-2015 estimates are analyzed in Sect. 3.3 and 3.4. Figure S2 in the supplement shows the time-series of isotopic signatures and illustrates this choice.

Figure 6 shows global and regional increments from the NOISO and REF inversions relative to prior estimates. Hereinafter, these differences will be referred to as "REF increment" (REF - PRIOR) and "NOISO increment" (NOISO - PRIOR). The difference between both increments will be called an "increment difference". Note that prior emissions are identical for all configurations. At the global scale, the posterior total emission inferred with REF is 595.0 $\pm$ 1 $\mathrm{Tg\,yr^{-1}}$ and the difference between REF and NOISO is only 0.3 $\mathrm{Tg\,yr^{-1}}$, indicating that the isotopic constraint does not affect the total global emissions. A higher discrepancy between these two budgets would have indicated a malfunction in the system as the sinks are the same but this small value is likely caused by a slight difference in the fitting to the observations and/or by the spatial variability of the prescribed sink coupled with the relocation of emissions when the isotopic constraint is implemented. Thus, the additional isotopic constraint only relocates the emissions and also reallocates them between categories, as intended. All but one of the emission categories exhibit large changes between NOISO and REF : wetlands (WT), fossil fuels (FF), microbial (MC) and biofuels-biomass burning (BB) categories.

Global increment differences in MC (-6.4 $\mathrm{Tg\,yr^{-1}}$) and FF emissions (8.6 $\mathrm{Tg\,yr^{-1}}$) are mainly due to regional increment difference in China and Temperate Asia. MC regional increment difference is equal to -2.1 $\mathrm{Tg\,yr^{-1}}$ in Temperate Asia and -2.4 $\mathrm{Tg\,yr^{-1}}$ in China. Similarly, FF increment difference is equal to 1.5 $\mathrm{Tg\,yr^{-1}}$ in Temperate Asia and 5.0 $\mathrm{Tg\,yr^{-1}}$ in China. WT global increment difference (-5.7 $\mathrm{Tg\,yr^{-1}}$) is mainly due to differences in Canada (-2.0 $\mathrm{Tg\,yr^{-1}}$) and South America (-2.3 $\mathrm{Tg\,yr^{-1}}$) but other regions such as Russia, Temperate Asia and South-East Asia are involved. BB emissions are also modified when implementing the isotopic constraint. Their global increment difference is equal to 3.2 $\mathrm{Tg\,yr^{-1}}$ principally owing to increment differences in South-East Asia (1.7 $\mathrm{Tg\,yr^{-1}}$), Canada (0.4 $\mathrm{Tg\,yr^{-1}}$) and Africa (0.4 $\mathrm{Tg\,yr^{-1}}$). The Natural (NAT) category exhibit very little changes (less than 1 $\mathrm{Tg\,yr^{-1}}$), even in relative values (see Fig. S3 in the supplement).

S-group configurations infer results remaining consistent with REF, with only small variations depending on the category and the region (see Table S5 in the supplement). In particular, S1 provides roughly the same results as REF but with more iterations, highlighting again that offsetting the initial conditions can help to reduce the computational burden without affecting the results. On the contrary, T-group configurations are affecting the increments, although T1 and T2 configurations are generally much closer to REF than T3 and T4. T1 (yellow dot) and T2 (blue dot) exhibits differences with the S-group essentially in China where WT and FF increments are modified ($\sim$ -3 $\mathrm{Tg\,yr^{-1}}$). More importantly, almost freezing the isotopic signatures to their prior values in this system (T3 and T4) results in increment differences 3 to 4 times larger than with REF, i.e. more than 10 $\mathrm{Tg\,yr^{-1}}$ at the global scale. It highlights the dependence of the inferred CH_4 emissions to the prior source signatures

https://doi.org/10.5194/gmd-2021-106
Preprint. Discussion started: 28 May 2021

Geoscientific Model Development Discussions
Open Access
EGU

Table 3. Global methane emissions by source category and region ($TgCH_4\ yr^{-1}$) for the REF configuration. Uncertainties are reported as the [min–max] range of all configurations.

	Biofuels-Biomass burning	Microbial	Fossil Fuels	Natural	Wetlands	Total
U.S	1 [1 - 1]	22 [21 - 22]	14 [13 - 15]	2 [2 - 2]	17 [16 - 17]	56 [55 - 56]
Canada	2 [1 - 3]	2 [2 - 2]	2 [2 - 2]	1 [1 - 1]	21 [16 - 23]	29 [24 - 30]
South America	2 [2 - 3]	30 [29 - 31]	6 [6 - 6]	5 [5 - 5]	53 [50 - 55]	96 [93 - 99]
Africa	9 [8 - 10]	25 [25 - 26]	14 [13 - 15]	4 [4 - 4]	28 [26 - 28]	80 [80 - 80]
Europe	1 [1 - 1]	20 [19 - 20]	6 [6 - 7]	2 [2 - 2]	4 [4 - 4]	34 [33 - 34]
Russia	2 [2 - 2]	5 [5 - 5]	12 [12 - 13]	3 [3 - 3]	12 [11 - 13]	35 [34 - 36]
Temperate Asia	3 [3 - 3]	54 [51 - 56]	28 [27 - 31]	7 [7 - 7]	13 [11 - 13]	105 [104 - 106]
China	5 [5 - 5]	29 [26 - 32]	24 [19 - 33]	1 [1 - 1]	5 [5 - 5]	64 [61 - 70]
South East Asia	11 [9 - 18]	23 [22 - 23]	8 [7 - 8]	4 [3 - 4]	22 [21 - 23]	66 [66 - 72]
Oceania	1 [0 - 1]	4 [4 - 5]	2 [2 - 2]	1 [1 - 1]	3 [3 - 3]	11 [11 - 11]
Others	1 [1 - 1]	4 [4 - 4]	5 [5 - 5]	8 [8 - 8]	2 [2 - 2]	19 [19 - 19]
Global	37 [33 - 47]	220 [210 - 226]	119 [111 - 134]	38 [38 - 39]	180 [167 - 185]	594 [594 - 597]

estimates. In other words, the quality of isotopic signature (values and distributions) appears to be critical for the robustness of the system's source estimates.

3.4 Global and regional source signature increments

Source isotopic signatures are also optimized by the system. Figure 7 provides the flux-weighted source isotopic signatures for different regions. It shows the difference between REF posterior and prior estimates.

All source signature are shifted upwards by the inversions, in order to correct the too strong negative trend in $\delta^{13}C(CH_4)$. At the global scale, flux-weighted source signatures of WT, FF, MC and BB are increased by 1.7, 0.5, 0.9 and 0.5 ‰, respectively. The global source signature is increased from -53.9 ‰ (prior) to -52.6 $\pm$ 0.2 ‰ (posterior) depending on the configuration (see Table S6). The posterior global signature is strongly dependent on the total fractionation effect. This effect tends to deplete air in $^{13}CH_4$, shifting the $\delta^{13}C(CH_4)$ to more positive values as the CH_4 molecules emitted by the sources are removed from the atmosphere. The total fractionation effect depends on 1) the prescribed OH, $O(^1D)$ and Cl concentrations and 2) the prescribed KIE values associated to the sinks (see Text S2 in the supplement). As the fractionation effect is the same for all configurations, the posterior global source signatures are very close.

The WT source signature exhibits the larger upward shift, from a global value of -60.8 ‰ to -59.1 ‰. This large difference for an average signature is due to upward shifts in Boreal regions (North America, Russia) but also in South America and Temperate Asia. The MC source signature is increased by 0.9 ‰ mainly due to changes in Asia. The FF source signature is increased by 0.5 ‰ globally due to a large increment in China (+ 1.2 ‰). Finally, the BB source signature is reevaluated in South-East Asia (+ 1.4 ‰) and Canada (+ 0.8 ‰).

These changes are consistent within the S-group (see blue errorbars in Fig. 7), although small variations are visible (e.g. $\pm$ 0.3 ‰ for WT in Canada). The source signature is therefore modified nearly to the same extent in all regions, no matter which

https://doi.org/10.5194/gmd-2021-106
Preprint. Discussion started: 28 May 2021

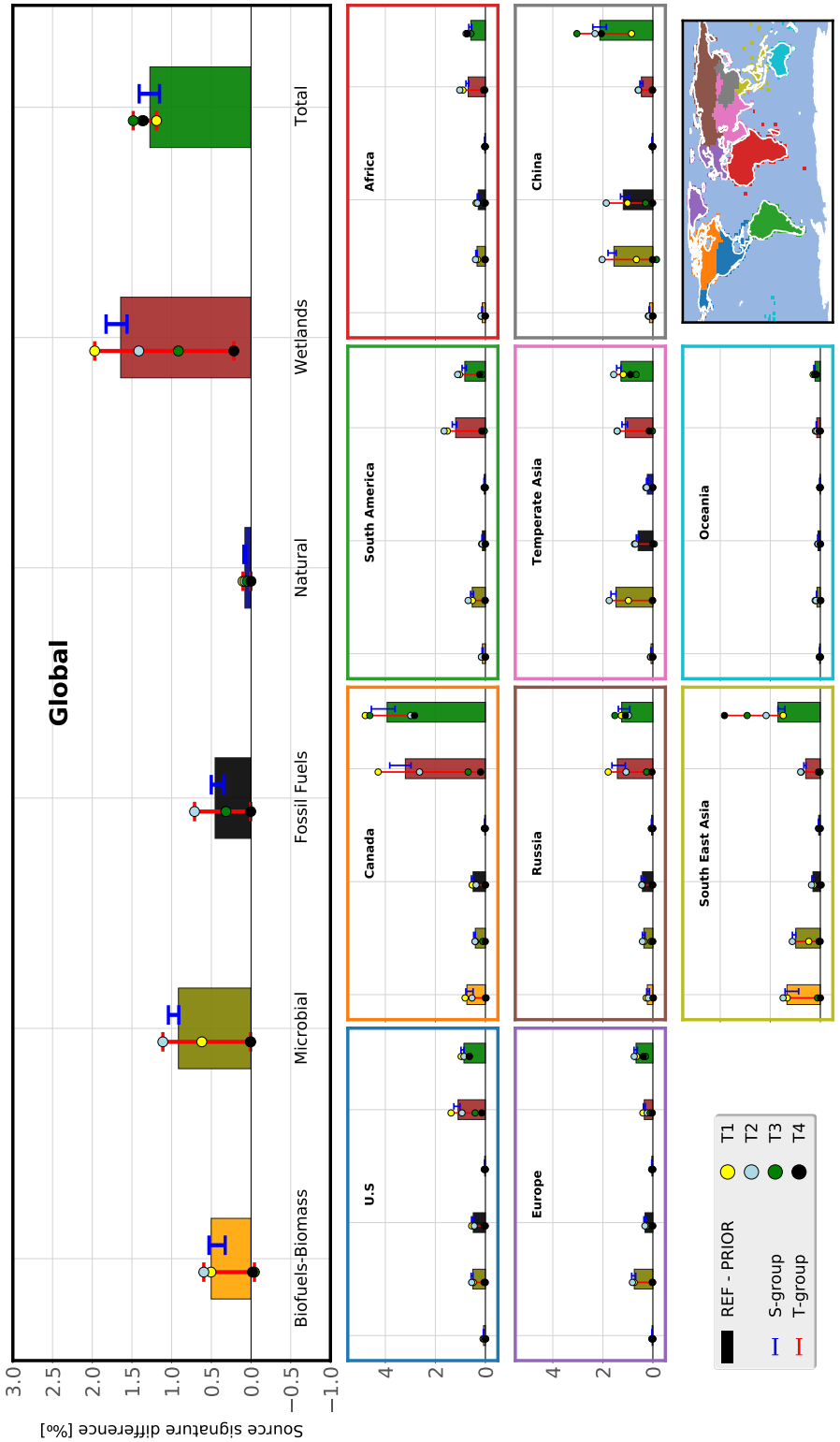

Figure 7. REF flux-weighted source signature increments for the period 2014-2015. Posterior fluxes are used to compute flux-weighted averages. The color-filled bars show the differences between REF posterior and prior estimates (REF increment). The upper panel refers to the global emissions. The lower panels refer to multiple regions of the globe. The regions are shown on the lower right panel. Red and blue error bars represent the minimum and maximum of the T-group and S-group, respectively. Circles on error bars show the results from the T-group.

https://doi.org/10.5194/gmd-2021-106
Preprint. Discussion started: 28 May 2021


Geoscientific Model Development Discussions

configuration in the S-group is analyzed. More details on prior and posterior values are given in the supplement (Table S6). T1 (yellow dot in Fig. 7), with more optimized categories than the others, shows small differences at global scale (less than 0.3 ‰ for all categories), although differences of more than 1 ‰ are visible in China. Therefore, increasing the number of degrees of freedom lead to similar flux estimates but can affect the signatures at regional scale.

T2 estimates are shifted upward to reach a less negative global source isotopic signature without getting closer to the regional distribution of the S-group. This is likely caused by the scarcity of $\delta^{13}C(CH_4)$ stations and correcting this behavior seems challenging without additional observations. The problem might be circumvented by using the region scale rather than the pixel scale to optimize isotopic signature values. Future inversions will test this assumption.

3.5 Posterior uncertainties

Formally, posterior uncertainties are given by the Hessian of the cost function. This matrix can hardly be computed at an achievable cost considering the size of the inverse problem. Other means must be implemented to get posterior uncertainties such as estimating lower-rank approximation of the Hessian, using Monte-Carlo ensembles of variational inversion to represent the prior uncertainties or computing multiple configurations covering a given range of possibilities. Here, using multiple configurations provide insight into the posterior uncertainty (min-max range) associated with the posterior fluxes. WT, MC, FF and BB flux estimates (Table 3) exhibit an uncertainty of 10 %, 7 %, 19 % and 38 %, respectively. BB is the most uncertain estimate relatively to its intensity, although FF show the largest absolute uncertainty (23 $\mathrm{Tg\,yr^{-1}}$).

4 Conclusions

We present here a new variational inversion system designed to assimilate observations of both a specific trace gas and its isotopic data. This system allows to optimize both the tracer emissions and the associated isotopic signatures for multiple source categories. To test this system we have assimilated CH_4 and $\delta^{13}C(CH_4)$ data retrieved at different measurement sites over the globe.

Different configurations have been tested in order to assess the sensibility of the system to the setup. We have shown that offsetting the $\delta^{13}C(CH_4)$ initial conditions before the inversion (S1), using $\delta^{13}C(CH_4)$ curve fitting data instead of the original observations (S2) and reducing the prescribed uncertainties in the $\delta^{13}C(CH_4)$ observations (S3) have very little effect on the inferred fluxes (less than 2 $\mathrm{Tg\,yr^{-1}}$ for each category at global scale). However, offsetting the $\delta^{13}C(CH_4)$ initial conditions before the inversion results in a reduced computational time (21 less iterations).

Other setup choices have more influence on the results. Increasing the number of source categories (T1) requires more computational time (10 more iterations) to reach a cost function (and RMSE) reduction similar to REF. Moreover, although the global posterior emissions with an increased number of categories are very close to those inferred with REF (less than 1 $\mathrm{Tg\,yr^{-1}}$), the posterior isotopic signatures can be modified in some regions (more than 1 ‰ in China). Also, starting from mean global values for the source signatures (T2) makes the system unable to retrieve the regional-specific isotopic signatures from REF. Increasing the number of $\delta^{13}C(CH_4)$ observations could help to cope with this issue. Finally, configurations which

https://doi.org/10.5194/gmd-2021-106
Preprint. Discussion started: 28 May 2021


Geoscientific Model Development Discussions

constrain the source signatures (T3-T4) show differences in global flux estimates of more than 10 $\mathrm{Tg\,yr^{-1}}$, compared to REF. This emphasizes the need for good prior source signature estimates.

The major caveat of this inversion system is undoubtedly the large computational burden of a full minimization process. At least 40 iterations appear to be necessary to reach a satisfying convergence state at the regional scale. For the LMDz-SACS model, a maximum of 8 CPUs can be run in parallel, resulting in an elapsed time of 5-6 weeks to run one of the inversions of this study. A new generation of transport models such as DYNAMICO (Dubos et al., 2015) could help to address this problem in the future by allowing more processors to run in parallel. In addition, variational inversions as implemented in the CIF are not enabled to provide a quantification (even approximated) of the posterior uncertainties. Dedicated efforts need to be done to address this issue in the future, at an achievable numerical cost.

This system is implemented within the CIF framework and can therefore be used for inversions with the various CTMs embedded in the CIF, provided the adjoint codes of the models exist. Due to the variational method benefits, the efforts dedicated to the preparation of inputs do not scale with either the size of the observational datasets or the length of the simulation time-window. Therefore, this system is very powerful and is particularly relevant to study in a consistent way the influence of multiple physical parameters on atmospheric isotopic ratios, such as the transport, the isotopic signatures, the emission scenarios, the KIE values, etc. We did not try to assess here the sensitivity of the system to these parameters as only technical aspects of the system were tested. This will be part of a future analysis.

$\delta^{13}\mathrm{C}(\mathrm{CH_4})$ is not the only isotopic data that can be assimilated in such a system. Many $\delta\mathrm{D}(\mathrm{CH_4})$ observations have also been retrieved during the period 2004-2010 at many different locations. These isotopic values can provide additional information that can further help to discriminate the co-emitted $\mathrm{CH_4}$ fluxes (Rigby et al., 2012). Moreover, ethane ($\mathrm{C_2H_6}$) is co-emitted with $\mathrm{CH_4}$ by fossil fuel extraction and distribution (Kort et al., 2016; Smith et al., 2015) and observations are available at a multitude of sites since the early 1980s. Therefore, assimilating this data can provide additional constraint. The system will therefore be improved in the future in order to assimilate $\delta^{13}\mathrm{C}(\mathrm{CH_4})$, $\delta\mathrm{D}(\mathrm{CH_4})$ and $\mathrm{C_2H_6}$ observations together.

Data availability. The CIF codes and documentation pages are available here: community-inversion.eu.

Author contributions. JT implemented the variational inversion system within the CIF with the precious help of AB. JT designed, run and analyzed the tested configurations. AB, MS, IP and PB provided scientific and technical expertise. They also contributed to the analysis of this work. BV and SEM provided scientific expertise regarding $\delta^{13}\mathrm{C}(\mathrm{CH_4})$ observations. JT prepared the manuscript with contributions from all co-authors.

Competing interests. The authors declare that they have no conflict of interest.

https://doi.org/10.5194/gmd-2021-106
Preprint. Discussion started: 28 May 2021

Acknowledgements. This work was supported by the CEA (Commissariat à l'Energie Atomique et aux Energies Alternatives). The study extensively relies on the meteorological data provided by the ECMWF. Calculations were performed using the computing resources of LSCE, maintained by François Marabelle and the LSCE IT team. We are grateful to many station maintainers that provided the CH_4 data: **For AGAGE network** - AGAGE is supported principally by NASA (USA) grants to MIT and SIO, and also by: BEIS (UK) and NOAA (USA) grants to Bristol University; CSIRO and BoM (Australia): FOEN grants to Empa (Switzerland); NILU (Norway); SNU (Korea); CMA (China); NIES (Japan); and Urbino University (Italy); **For South African Weather Service Cape Point GAW station** - We thank Casper Labuschagne, Thumeka Mkololo and Warren Joubert ; **For EC network** - We thank Doug Worthy; **For MGO network** - We thank Nina Paramonova and Victor Ivakhov; **For AMY network** - We thank Haeyoung Lee and Sepyo Lee - The AMY data was funded by the Korea Meteorological Administration Research and Development Program under grant KMA2018-00522; **For ENEA network** - We thank Alcide Disarra, Salvatore Piacentino and Damiano Sferlazzo; **For EMPA network** - We thank Martin Steinbacher and Brigitte Buchmann - The CH_4 measurements at JFJ are run by EMPA in collaboration with FOEN and are also supported by ICOS-CH; **For BMKG-EMPA network** - We thank Martin Steinbacher, Alberth Christian and Sugeng Nugroho - The CH_4 measurements at BKT are run by BMKG in collaboration with EMPA;

https://doi.org/10.5194/gmd-2021-106
Preprint. Discussion started: 28 May 2021

References

Berchet, A., Sollum, E., Thompson, R. L., Pison, I., Thanwerdas, J., Broquet, G., Chevallier, F., Aalto, T., Bergamaschi, P., Brunner, D., Engelen, R., Fortems-Cheiney, A., Gerbig, C., Groot Zwaaftink, C., Haussaire, J.-M., Henne, S., Houweling, S., Karstens, U., Kutsch, W. L., Luijkx, I. T., Monteil, G., Palmer, P. I., van Peet, J. C. A., Peters, W., Peylin, P., Potier, E., Rödenbeck, C., Saunois, M., Scholze, M., Tsuruta, A., and Zhao, Y.: The Community Inversion Framework v1.0: a unified system for atmospheric inversion studies, Geoscientific Model Development Discussions, pp. 1–41, https://doi.org/https://doi.org/10.5194/gmd-2020-407, https://gmd.copernicus.org/preprints/gmd-2020-407/, 2020.

Bergamaschi, P., Krol, M., Meirink, J. F., Dentener, F., Segers, A., Aardenne, J. v., Monni, S., Vermeulen, A. T., Schmidt, M., Ramonet, M., Yver, C., Meinhardt, F., Nisbet, E. G., Fisher, R. E., O'Doherty, S., and Dlugokencky, E. J.: Inverse modeling of European CH_4 emissions 2001–2006, Journal of Geophysical Research: Atmospheres, 115, https://doi.org/https://doi.org/10.1029/2010JD014180, https://agupubs.onlinelibrary.wiley.com/doi/abs/10.1029/2010JD014180, 2010.

Bergamaschi, P., Houweling, S., Segers, A., Krol, M., Frankenberg, C., Scheepmaker, R. A., Dlugokencky, E., Wofsy, S. C., Kort, E. A., Sweeney, C., Schuck, T., Brenninkmeijer, C., Chen, H., Beck, V., and Gerbig, C.: Atmospheric CH_4 in the first decade of the 21st century: Inverse modeling analysis using SCIAMACHY satellite retrievals and NOAA surface measurements, Journal of Geophysical Research: Atmospheres, 118, 7350–7369, https://doi.org/10.1002/jgrd.50480, http://agupubs.onlinelibrary.wiley.com/doi/abs/10.1002/jgrd.50480, 2013.

Bergamaschi, P., Karstens, U., Manning, A. J., Saunois, M., Tsuruta, A., Berchet, A., Vermeulen, A. T., Arnold, T., Janssens-Maenhout, G., Hammer, S., Levin, I., Schmidt, M., Ramonet, M., Lopez, M., Lavric, J., Aalto, T., Chen, H., Feist, D. G., Gerbig, C., Haszpra, L., Hermansen, O., Manca, G., Moncrieff, J., Meinhardt, F., Necki, J., Galkowski, M., O'Doherty, S., Paramonova, N., Scheeren, H. A., Steinbacher, M., and Dlugokencky, E.: Inverse modelling of European CH_4 emissions during 2006–2012 using different inverse models and reassessed atmospheric observations, Atmospheric Chemistry and Physics, 18, 901–920, https://doi.org/https://doi.org/10.5194/acp-18-901-2018, https://www.atmos-chem-phys.net/18/901/2018/, 2018.

Bousquet, P., Ciais, P., Miller, J. B., Dlugokencky, E. J., Hauglustaine, D. A., Prigent, C., Van der Werf, G. R., Peylin, P., Brunke, E.-G., Carouge, C., Langenfelds, R. L., Lathière, J., Papa, F., Ramonet, M., Schmidt, M., Steele, L. P., Tyler, S. C., and White, J.: Contribution of anthropogenic and natural sources to atmospheric methane variability, Nature, 443, 439–443, https://doi.org/10.1038/nature05132, http://www.nature.com/articles/nature05132, 2006.

Chang, J., Peng, S., Ciais, P., Saunois, M., Dangal, S. R. S., Herrero, M., Havlík, P., Tian, H., and Bousquet, P.: Revisiting enteric methane emissions from domestic ruminants and their $\delta^{13}CCH_4$ source signature, Nature Communications, 10, 3420, https://doi.org/10.1038/s41467-019-11066-3, http://www.nature.com/articles/s41467-019-11066-3, 2019.

Chevallier, F., Fisher, M., Peylin, P., Serrar, S., Bousquet, P., Bréon, F.-M., Chédin, A., and Ciais, P.: Inferring CO_2 sources and sinks from satellite observations: Method and application to TOVS data, Journal of Geophysical Research, 110, https://doi.org/10.1029/2005JD006390, http://doi.wiley.com/10.1029/2005JD006390, 2005.

Craig, H.: Isotopic standards for carbon and oxygen and correction factors for mass-spectrometric analysis of carbon dioxide, Geochimica et Cosmochimica Acta, 12, 133–149, https://doi.org/10.1016/0016-7037(57)90024-8, http://www.sciencedirect.com/science/article/pii/0016703757900248, 1957.

https://doi.org/10.5194/gmd-2021-106
Preprint. Discussion started: 28 May 2021

Dubos, T., Dubey, S., Tort, M., Mittal, R., Meurdesoif, Y., and Hourdin, F.: DYNAMICO-1.0, an icosahedral hydrostatic dynamical core designed for consistency and versatility, Geoscientific Model Development, 8, 3131–3150, https://doi.org/10.5194/gmd-8-3131-2015, https://gmd.copernicus.org/articles/8/3131/2015/, 2015.

Enting, I. G. and Newsam, G. N.: Atmospheric constituent inversion problems: Implications for baseline monitoring, Journal of Atmospheric Chemistry, 11, 69–87, https://doi.org/10.1007/BF00053668, http://link.springer.com/10.1007/BF00053668, 1990.

Etiope, G.: Natural Gas Seepage: The Earth's Hydrocarbon Degassing, Springer International Publishing, https://www.springer.com/gp/book/9783319146003, 2015.

Etminan, M., Myhre, G., Highwood, E. J., and Shine, K. P.: Radiative forcing of carbon dioxide, methane, and nitrous oxide: A significant revision of the methane radiative forcing, Geophysical Research Letters, 43, 12,614–12,623, https://doi.org/https://doi.org/10.1002/2016GL071930, http://agupubs.onlinelibrary.wiley.com/doi/abs/10.1002/2016GL071930, 2016.

Fletcher, S. E. M., Tans, P. P., Bruhwiler, L. M., Miller, J. B., and Heimann, M.: CH_4 sources estimated from atmospheric observations of CH_4 and its $^{13}C/^{12}C$ isotopic ratios: 2. Inverse modeling of CH_4 fluxes from geographical regions, Global Biogeochemical Cycles, 18, https://doi.org/10.1029/2004GB002224, https://agupubs.onlinelibrary.wiley.com/doi/abs/10.1029/2004GB002224, 2004.

Fujita, R., Morimoto, S., Maksyutov, S., Kim, H.-S., Arshinov, M., Brailsford, G., Aoki, S., and Nakazawa, T.: Global and Regional CH_4 Emissions for 1995–2013 Derived From Atmospheric CH_4, δ^{13}C-CH_4, and δD-CH_4 Observations and a Chemical Transport Model, Journal of Geophysical Research: Atmospheres, 125, e2020JD032 903, https://doi.org/https://doi.org/10.1029/2020JD032903, https://agupubs.onlinelibrary.wiley.com/doi/abs/10.1029/2020JD032903, 2020.

Ganesan, A. L., Stell, A. C., Gedney, N., Comyn-Platt, E., Hayman, G., Rigby, M., Poulter, B., and Hornibrook, E. R. C.: Spatially Resolved Isotopic Source Signatures of Wetland Methane Emissions, Geophysical Research Letters, 45, 3737–3745, https://doi.org/10.1002/2018GL077536, https://agupubs.onlinelibrary.wiley.com/doi/abs/10.1002/2018GL077536, 2018.

Gilbert, J. C. and Lemaréchal, C.: Some numerical experiments with variable-storage quasi-Newton algorithms, Mathematical Programming, 45, 407–435, https://doi.org/10.1007/BF01589113, https://doi.org/10.1007/BF01589113, 1989.

Gurney, K. R., Law, R. M., Denning, A. S., Rayner, P. J., Baker, D., Bousquet, P., Bruhwiler, L., Chen, Y.-H., Ciais, P., Fan, S., Fung, I. Y., Gloor, M., Heimann, M., Higuchi, K., John, J., Maki, T., Maksyutov, S., Masarie, K., Peylin, P., Prather, M., Sarmiento, J., Taguchi, S., Takahashi, T., and Yuen, C.-W.: Towards robust regional estimates of CO_2 sources and sinks using atmospheric transport models, 415, 5, 2002.

Hourdin, F., Musat, I., Bony, S., Braconnot, P., Codron, F., Dufresne, J.-L., Fairhead, L., Filiberti, M.-A., Friedlingstein, P., Grandpeix, J.-Y., Krinner, G., LeVan, P., Li, Z.-X., and Lott, F.: The LMDZ4 general circulation model: climate performance and sensitivity to parametrized physics with emphasis on tropical convection, Climate Dynamics, 27, 787–813, https://doi.org/10.1007/s00382-006-0158-0, http://link.springer.com/10.1007/s00382-006-0158-0, 2006.

Houweling, S., Bergamaschi, P., Chevallier, F., Heimann, M., Kaminski, T., Krol, M., Michalak, A. M., and Patra, P.: Global inverse modeling of CH_4 sources and sinks: an overview of methods, Atmospheric Chemistry and Physics, 17, 235–256, https://doi.org/https://doi.org/10.5194/acp-17-235-2017, https://www.atmos-chem-phys.net/17/235/2017/, 2017.

Ide, K., Courtier, P., Ghil, M., and Lorenc, A. C.: Unified Notation for Data Assimilation : Operational, Sequential and Variational (gtSpecial IssueltData Assimilation in Meteology and Oceanography: Theory and Practice), Journal of the Meteorological Society of Japan. Ser. II, 75, 181–189, https://doi.org/10.2151/jmsj1965.75.1B_181, 1997.

Janssens-Maenhout, G., Crippa, M., Guizzardi, D., Muntean, M., Schaaf, E., Dentener, F., Bergamaschi, P., Pagliari, V., Olivier, J. G. J., Peters, J. A. H. W., Aardenne, J. A. v., Monni, S., Doering, U., and Petrescu, A. M. R.: EDGAR v4.3.2 Global Atlas of

the three major Greenhouse Gas Emissions for the period 1970–2012, Earth System Science Data Discussions, pp. 1–55, https://doi.org/https://doi.org/10.5194/essd-2017-79, https://www.earth-syst-sci-data-discuss.net/essd-2017-79/, 2017.

Kirschke, S., Bousquet, P., Ciais, P., Saunois, M., Canadell, J. G., Dlugokencky, E. J., Bergamaschi, P., Bergmann, D., Blake, D. R., Bruhwiler, L., Cameron-Smith, P., Castaldi, S., Chevallier, F., Feng, L., Fraser, A., Heimann, M., Hodson, E. L., Houweling, S., Josse, B., Fraser, P. J., Krummel, P. B., Lamarque, J.-F., Langenfelds, R. L., Le Quéré, C., Naik, V., O'Doherty, S., Palmer, P. I., Pison, I., Plummer, D., Poulter, B., Prinn, R. G., Rigby, M., Ringeval, B., Santini, M., Schmidt, M., Shindell, D. T., Simpson, I. J., Spahni, R., Steele, L. P., Strode, S. A., Sudo, K., Szopa, S., van der Werf, G. R., Voulgarakis, A., van Weele, M., Weiss, R. F., Williams, J. E., and Zeng, G.: Three decades of global methane sources and sinks, Nature Geoscience, 6, 813–823, https://doi.org/10.1038/ngeo1955, http://www.nature.com/articles/ngeo1955, 2013.

Kort, E. A., Smith, M. L., Murray, L. T., Gvakharia, A., Brandt, A. R., Peischl, J., Ryerson, T. B., Sweeney, C., and Travis, K.: Fugitive emissions from the Bakken shale illustrate role of shale production in global ethane shift, Geophysical Research Letters, 43, 4617–4623, https://doi.org/https://doi.org/10.1002/2016GL068703, https://agupubs.onlinelibrary.wiley.com/doi/abs/10.1002/2016GL068703, 2016.

Lambert, G. and Schmidt, S.: Reevaluation of the oceanic flux of methane: Uncertainties and long term variations, Chemosphere, 26, 579–589, https://doi.org/10.1016/0045-6535(93)90443-9, http://www.sciencedirect.com/science/article/pii/0045653593904439, 1993.

Liu, X., Weinbren, A. L., Chang, H., Tadić, J., Mountain, M. E., Trudeau, M. E., Andrews, A. E., Chen, Z., and Miller, S. M.: Data reduction for inverse modeling: an adaptive approach v1.0, Geoscientific Model Development Discussions, pp. 1–21, https://doi.org/10.5194/gmd-2020-246, https://gmd.copernicus.org/preprints/gmd-2020-246/, 2020.

Locatelli, R., Bousquet, P., Chevallier, F., Fortems-Cheney, A., Szopa, S., Saunois, M., Agusti-Panareda, A., Bergmann, D., Bian, H., Cameron-Smith, P., Chipperfield, M. P., Gloor, E., Houweling, S., Kawa, S. R., Krol, M., Patra, P. K., Prinn, R. G., Rigby, M., Saito, R., and Wilson, C.: Impact of transport model errors on the global and regional methane emissions estimated by inverse modelling, Atmospheric Chemistry and Physics, 13, 9917–9937, https://doi.org/https://doi.org/10.5194/acp-13-9917-2013, https://www.atmos-chem-phys.net/13/9917/2013/, 2013.

Locatelli, R., Bousquet, P., Saunois, M., Chevallier, F., and Cressot, C.: Sensitivity of the recent methane budget to LMDz sub-grid-scale physical parameterizations, Atmospheric Chemistry and Physics, 15, 9765–9780, https://doi.org/10.5194/acp-15-9765-2015, http://www.atmos-chem-phys.net/15/9765/2015/, 2015.

Louis, J.-F.: A parametric model of vertical eddy fluxes in the atmosphere, Boundary-Layer Meteorology, 17, 187–202, https://doi.org/10.1007/BF00117978, https://doi.org/10.1007/BF00117978, 1979.

Masarie, K. A. and Tans, P. P.: Extension and integration of atmospheric carbon dioxide data into a globally consistent measurement record, Journal of Geophysical Research: Atmospheres, 100, 11 593–11 610, https://doi.org/10.1029/95JD00859, http://agupubs.onlinelibrary.wiley.com/doi/abs/10.1029/95JD00859, 1995.

McNorton, J., Wilson, C., Gloor, M., Parker, R. J., Boesch, H., Feng, W., Hossaini, R., and Chipperfield, M. P.: Attribution of recent increases in atmospheric methane through 3-D inverse modelling, Atmospheric Chemistry and Physics, 18, 18 149–18 168, https://doi.org/https://doi.org/10.5194/acp-18-18149-2018, https://www.atmos-chem-phys.net/18/18149/2018/, 2018.

Menut, L., Bessagnet, B., Khvorostyanov, D., Beekmann, M., Blond, N., Colette, A., Coll, I., Curci, G., Foret, G., Hodzic, A., Mailler, S., Meleux, F., Monge, J.-L., Pison, I., Siour, G., Turquety, S., Valari, M., Vautard, R., and Vivanco, M. G.: CHIMERE 2013: a model for regional atmospheric composition modelling, Geoscientific Model Development, 6, 981–1028, https://doi.org/10.5194/gmd-6-981-2013, https://www.geosci-model-dev.net/6/981/2013/, 2013.

https://doi.org/10.5194/gmd-2021-106
Preprint. Discussion started: 28 May 2021

Neef, L., Weele, M. v., and Velthoven, P. v.: Optimal estimation of the present-day global methane budget, Global Biogeochemical Cycles, 24, https://doi.org/10.1029/2009GB003661, https://agupubs.onlinelibrary.wiley.com/doi/abs/10.1029/2009GB003661, 2010.

Newsam, G. N. and Enting, I. G.: Inverse problems in atmospheric constituent studies. I. Determination of surface sources under a diffusive transport approximation, Inverse Problems, 4, 1037–1054, https://doi.org/10.1088/0266-5611/4/4/008, http://stacks.iop.org/0266-5611/4/i=4/a=008?key=crossref.5679eadd6a85e6ba1edce2d2490b2836, 1988.

Nisbet, E. G., Manning, M. R., Dlugokencky, E. J., Fisher, R. E., Lowry, D., Michel, S. E., Myhre, C. L., Platt, S. M., Allen, G., Bousquet, P., Brownlow, R., Cain, M., France, J. L., Hermansen, O., Hossaini, R., Jones, A. E., Levin, I., Manning, A. C., Myhre, G., Pyle, J. A., Vaughn, B. H., Warwick, N. J., and White, J. W. C.: Very Strong Atmospheric Methane Growth in the 4 Years 2014–2017: Implications for the Paris Agreement, Global Biogeochemical Cycles, 33, 318–342, https://doi.org/10.1029/2018GB006009, https://agupubs.onlinelibrary.wiley.com/doi/abs/10.1029/2018GB006009, 2019.

Patra, P. K., Houweling, S., Krol, M., Bousquet, P., Belikov, D., Bergmann, D., Bian, H., Cameron-Smith, P., Chipperfield, M. P., Corbin, K., Fortems-Cheiney, A., Fraser, A., Gloor, E., Hess, P., Ito, A., Kawa, S. R., Law, R. M., Loh, Z., Maksyutov, S., Meng, L., Palmer, P. I., Prinn, R. G., Rigby, M., Saito, R., and Wilson, C.: TransCom model simulations of CH_4 and related species: linking transport, surface flux and chemical loss with CH_4 variability in the troposphere and lower stratosphere, Atmospheric Chemistry and Physics, 11, 12 813–12 837, https://doi.org/10.5194/acp-11-12813-2011, http://www.atmos-chem-phys.net/11/12813/2011/, 2011.

Peters, W., Miller, J. B., Whitaker, J., Denning, A. S., Hirsch, A., Krol, M. C., Zupanski, D., Bruhwiler, L., and Tans, P. P.: An ensemble data assimilation system to estimate CO_2 surface fluxes from atmospheric trace gas observations, Journal of Geophysical Research: Atmospheres, 110, https://doi.org/https://doi.org/10.1029/2005JD006157, https://agupubs.onlinelibrary.wiley.com/doi/abs/10.1029/2005JD006157, 2005.

Pison, I., Bousquet, P., Chevallier, F., Szopa, S., and Hauglustaine, D.: Multi-species inversion of CH_4, CO and H2 emissions from surface measurements, Atmos. Chem. Phys., p. 17, 2009.

Poulter, B., Bousquet, P., Canadell, J. G., Ciais, P., Peregon, A., Saunois, M., Arora, V. K., Beerling, D. J., Brovkin, V., Jones, C. D., Joos, F., Gedney, N., Ito, A., Kleinen, T., Koven, C. D., McDonald, K., Melton, J. R., Peng, C., Peng, S., Prigent, C., Schroeder, R., Riley, W. J., Saito, M., Spahni, R., Tian, H., Taylor, L., Viovy, N., Wilton, D., Wiltshire, A., Xu, X., Zhang, B., Zhang, Z., and Zhu, Q.: Global wetland contribution to 2000–2012 atmospheric methane growth rate dynamics, Environmental Research Letters, 12, 094 013, https://doi.org/10.1088/1748-9326/aa8391, https://doi.org/10.1088%2F1748-9326%2Faa8391, 2017.

Rice, A. L., Butenhoff, C. L., Teama, D. G., Röger, F. H., Khalil, M. A. K., and Rasmussen, R. A.: Atmospheric methane isotopic record favors fossil sources flat in 1980s and 1990s with recent increase, Proceedings of the National Academy of Sciences, 113, 10 791–10 796, https://doi.org/10.1073/pnas.1522923113, https://www.pnas.org/content/113/39/10791, 2016.

Rigby, M., Manning, A. J., and Prinn, R. G.: The value of high-frequency, high-precision methane isotopologue measurements for source and sink estimation, Journal of Geophysical Research: Atmospheres, 117, https://doi.org/10.1029/2011JD017384, https://agupubs.onlinelibrary.wiley.com/doi/abs/10.1029/2011JD017384, 2012.

Rigby, M., Montzka, S. A., Prinn, R. G., White, J. W. C., Young, D., O'Doherty, S., Lunt, M. F., Ganesan, A. L., Manning, A. J., Simmonds, P. G., Salameh, P. K., Harth, C. M., Mühle, J., Weiss, R. F., Fraser, P. J., Steele, L. P., Krummel, P. B., McCulloch, A., and Park, S.: Role of atmospheric oxidation in recent methane growth, Proceedings of the National Academy of Sciences, 114, 5373–5377, https://doi.org/10.1073/pnas.1616426114, http://www.pnas.org/lookup/doi/10.1073/pnas.1616426114, 2017.

Rodenbeck, C., Houweling, S., Gloor, M., and Heimann, M.: CO_2 flux history 1982–2001 inferred from atmospheric data using a global inversion of atmospheric transport, Atmos. Chem. Phys., p. 46, 2003.

https://doi.org/10.5194/gmd-2021-106
Preprint. Discussion started: 28 May 2021

Saunois, M., Bousquet, P., Poulter, B., Peregon, A., Ciais, P., Canadell, J. G., Dlugokencky, E. J., Etiope, G., Bastviken, D., Houweling, S., Janssens-Maenhout, G., Tubiello, F. N., Castaldi, S., Jackson, R. B., Alexe, M., Arora, V. K., Beerling, D. J., Bergamaschi, P., Blake, D. R., Brailsford, G., Bruhwiler, L., Crevoisier, C., Crill, P., Covey, K., Frankenberg, C., Gedney, N., Höglund-Isaksson, L., Ishizawa, M., Ito, A., Joos, F., Kim, H.-S., Kleinen, T., Krummel, P., Lamarque, J.-F., Langenfelds, R., Locatelli, R., Machida, T., Maksyutov, S., Melton, J. R., Morino, I., Naik, V., O'Doherty, S., Parmentier, F.-J. W., Patra, P. K., Peng, C., Peng, S., Peters, G. P., Pison, I., Prinn, R., Ramonet, M., Riley, W. J., Saito, M., Santini, M., Schroeder, R., Simpson, I. J., Spahni, R., Takizawa, A., Thornton, B. F., Tian, H., Tohjima, Y., Viovy, N., Voulgarakis, A., Weiss, R., Wilton, D. J., Wiltshire, A., Worthy, D., Wunch, D., Xu, X., Yoshida, Y., Zhang, B., Zhang, Z., and Zhu, Q.: Variability and quasi-decadal changes in the methane budget over the period 2000–2012, Atmospheric Chemistry and Physics, 17, 11 135–11 161, https://doi.org/https://doi.org/10.5194/acp-17-11135-2017, https://www.atmos-chem-phys.net/17/11135/2017/, 2017.

Saunois, M., Stavert, A. R., Poulter, B., Bousquet, P., Canadell, J. G., Jackson, R. B., Raymond, P. A., Dlugokencky, E. J., Houweling, S., Patra, P. K., Ciais, P., Arora, V. K., Bastviken, D., Bergamaschi, P., Blake, D. R., Brailsford, G., Bruhwiler, L., Carlson, K. M., Carrol, M., Castaldi, S., Chandra, N., Crevoisier, C., Crill, P. M., Covey, K., Curry, C. L., Etiope, G., Frankenberg, C., Gedney, N., Hegglin, M. I., Höglund-Isaksson, L., Hugelius, G., Ishizawa, M., Ito, A., Janssens-Maenhout, G., Jensen, K. M., Joos, F., Kleinen, T., Krummel, P. B., Langenfelds, R. L., Laruelle, G. G., Liu, L., Machida, T., Maksyutov, S., McDonald, K. C., McNorton, J., Miller, P. A., Melton, J. R., Morino, I., Müller, J., Murguia-Flores, F., Naik, V., Niwa, Y., Noce, S., O'Doherty, S., Parker, R. J., Peng, C., Peng, S., Peters, G. P., Prigent, C., Prinn, R., Ramonet, M., Regnier, P., Riley, W. J., Rosentreter, J. A., Segers, A., Simpson, I. J., Shi, H., Smith, S. J., Steele, L. P., Thornton, B. F., Tian, H., Tohjima, Y., Tubiello, F. N., Tsuruta, A., Viovy, N., Voulgarakis, A., Weber, T. S., van Weele, M., van der Werf, G. R., Weiss, R. F., Worthy, D., Wunch, D., Yin, Y., Yoshida, Y., Zhang, W., Zhang, Z., Zhao, Y., Zheng, B., Zhu, Q., Zhu, Q., and Zhuang, Q.: The Global Methane Budget 2000–2017, Earth System Science Data, 12, 1561–1623, https://doi.org/https://doi.org/10.5194/essd-12-1561-2020, https://essd.copernicus.org/articles/12/1561/2020/, 2020.

Schaefer, H., Fletcher, S. E. M., Veidt, C., Lassey, K. R., Brailsford, G. W., Bromley, T. M., Dlugokencky, E. J., Michel, S. E., Miller, J. B., Levin, I., Lowe, D. C., Martin, R. J., Vaughn, B. H., and White, J. W. C.: A 21st-century shift from fossil-fuel to biogenic methane emissions indicated by $^{13}CH_4$, Science, 352, 80–84, https://doi.org/10.1126/science.aad2705, https://science-sciencemag-org.insu.bib.cnrs.fr/content/352/6281/80, 2016.

Schwietzke, S., Sherwood, O. A., Bruhwiler, L. M. P., Miller, J. B., Etiope, G., Dlugokencky, E. J., Michel, S. E., Arling, V. A., Vaughn, B. H., White, J. W. C., and Tans, P. P.: Upward revision of global fossil fuel methane emissions based on isotope database, Nature, 538, 88–91, https://doi.org/10.1038/nature19797, http://www.nature.com/articles/nature19797, 2016.

Sherwood, O. A., Schwietzke, S., Arling, V. A., and Etiope, G.: Global Inventory of Gas Geochemistry Data from Fossil Fuel, Microbial and Burning Sources, version 2017, Earth System Science Data, 9, 639–656, https://doi.org/10.5194/essd-9-639-2017, https://www.earth-syst-sci-data.net/9/639/2017/, 2017.

Smith, M. L., Kort, E. A., Karion, A., Sweeney, C., Herndon, S. C., and Yacovitch, T. I.: Airborne Ethane Observations in the Barnett Shale: Quantification of Ethane Flux and Attribution of Methane Emissions, Environmental Science & Technology, 49, 8158–8166, https://doi.org/10.1021/acs.est.5b00219, https://doi.org/10.1021/acs.est.5b00219, 2015.

Tans, P. P.: A note on isotopic ratios and the global atmospheric methane budget, Global Biogeochemical Cycles, 11, 77–81, https://doi.org/10.1029/96GB03940, https://agupubs.onlinelibrary.wiley.com/doi/abs/10.1029/96GB03940, 1997.

Thompson, R. L., Nisbet, E. G., Pisso, I., Stohl, A., Blake, D., Dlugokencky, E. J., Helmig, D., and White, J. W. C.: Variability in Atmospheric Methane From Fossil Fuel and Microbial Sources Over the Last Three Decades, Geophysical Research Letters, 45, 11,499–11,508, https://doi.org/10.1029/2018GL078127, https://agupubs.onlinelibrary.wiley.com/doi/abs/10.1029/2018GL078127, 2018.

https://doi.org/10.5194/gmd-2021-106
Preprint. Discussion started: 28 May 2021

Tiedtke, M.: A Comprehensive Mass Flux Scheme for Cumulus Parameterization in Large-Scale Models, Monthly Weather Review, 117, 1779–1800, https://doi.org/10.1175/1520-0493(1989)117<1779:ACMFSF>2.0.CO;2, https://journals.ametsoc.org/doi/abs/10.1175/1520-0493%281989%29117%3C1779%3AACMFSF%3E2.0.CO%3B2, 1989.

Turner, A. J., Frankenberg, C., Wennberg, P. O., and Jacob, D. J.: Ambiguity in the causes for decadal trends in atmospheric methane and hydroxyl, p. 6, 2017.

van der Werf, G. R., Randerson, J. T., Giglio, L., van Leeuwen, T. T., Chen, Y., Rogers, B. M., Mu, M., van Marle, M. J. E., Morton, D. C., Collatz, G. J., Yokelson, R. J., and Kasibhatla, P. S.: Global fire emissions estimates during 1997–2016, Earth System Science Data, 9, 697–720, https://doi.org/10.5194/essd-9-697-2017, https://www.earth-syst-sci-data.net/9/697/2017/, 2017.

Yver, C. E., Pison, I. C., Fortems-Cheiney, A., Schmidt, M., Chevallier, F., Ramonet, M., Jordan, A., Søvde, O. A., Engel, A., Fisher, R. E., Lowry, D., Nisbet, E. G., Levin, I., Hammer, S., Necki, J., Bartyzel, J., Reimann, S., Vollmer, M. K., Steinbacher, M., Aalto, T., Maione, M., Arduini, J., O'Doherty, S., Grant, A., Sturges, W. T., Forster, G. L., Lunder, C. R., Privalov, V., Paramonova, N., Werner, A., and Bousquet, P.: A new estimation of the recent tropospheric molecular hydrogen budget using atmospheric observations and variational inversion, Atmospheric Chemistry and Physics, 11, 3375–3392, https://doi.org/10.5194/acp-11-3375-2011, https://www.atmos-chem-phys.net/11/3375/2011/, 2011.

Zazzeri, G., Lowry, D., Fisher, R. E., France, J. L., Lanoisellé, M., Kelly, B. F. J., Necki, J. M., Iverach, C. P., Ginty, E., Zimnoch, M., Jasek, A., and Nisbet, E. G.: Carbon isotopic signature of coal-derived methane emissions to the atmosphere:from coalification to alteration, Atmospheric Chemistry and Physics, 16, 13 669–13 680, https://doi.org/10.5194/acp-16-13669-2016, https://www.atmos-chem-phys.net/16/13669/2016/, 2016.

Zupanski, D., Hou, A. Y., Zhang, S. Q., Zupanski, M., Kummerow, C. D., and Cheung, S. H.: Applications of information theory in ensemble data assimilation, Quarterly Journal of the Royal Meteorological Society, 133, 1533–1545, https://doi.org/https://doi.org/10.1002/qj.123, http://rmets.onlinelibrary.wiley.com/doi/abs/10.1002/qj.123, 2007.